

PONTIFICIA UNIVERSIDAD CATÓLICA DEL PERÚ

ESCUELA DE POSGRADO



Recasting and Validating a Search for Long Lived Particles using a CalRatio trigger in the

ATLAS experiment

Tesis para obtener el grado de Maestra en Física que presenta:

Lucía Ximena Coll Saravia

Asesor:

Joel Jones Pérez

Lima, 2023


Informe de Similitud

Yo, Joel Jones Pérez, docente de la Escuela de Posgrado de la Pontificia Universidad Católica del Perú, asesor de la tesis de investigación titulada "Recasting and validating a search for Long Lived Particles using a CalRatio trigger in the ATLAS experiment", de la autora Lucía Ximena Coll Saravia, dejo constancia de lo siguiente:

- El mencionado documento tiene un índice de puntuación de similitud de 27%. Así lo consigna el reporte de similitud emitido por el software *Turnitin* el 05/09/2023.
- He revisado con detalle dicho reporte y la Tesis o Trabajo de Suficiencia Profesional, y no se advierte indicios de plagio. La razón por el alto índice de puntuación se debe principalmente a que la misma Sra Coll escribió un trabajo de bachillerato previamente, del cual esta tesis se basa (11% de coincidencia). Dicho trabajo se encuentra citado en la tesis. En caso retirar la coincidencia, el índice se reduce a 16%.
- Las citas a otros autores y sus respectivas referencias cumplen con las pautas académicas.

Lugar y fecha:

Lima, 05/09/2023

Apellidos y nombres del asesor / de la asesora: Jones Pérez Joel	
DNI: 40711425	Firma 
ORCID: 0000-0002-2037-6369	

Abstract

The Standard Model (SM) of particle physics consists in a description of all the known elementary particles and their interactions. As far as it is known, the SM has passed all experimental tests, but presents some imperfections having no explanation for such as the presence of neutrino masses and the hierarchy problem. This encourages to probe theories beyond the Standard Model (BSM) that could bring solutions to these problems. An interesting proposal is to search for neutral long lived particles (LLPs). These type of particles have long decay lengths, can be generated by a variety of BSM models and could be detected in collider experiments by searching for displaced signals. The detection of the decay products of LLPs decays will contribute to the discovery of new physics.

The objective of this work is to upgrade and optimize the PUCP Toy Detector presented in [1], adapting the simulation to the ATLAS detector and adding new features as a Geant4 simulation of the calorimeter for calculating the energy deposits. And validating it by reproducing the result of the searches presented in [2]. We conclude that the PUCP Toy Detector is valid, well implemented, and will be a competitive tool for searching new models containing LLPs decaying inside the calorimeters in the future.

Magari qualche volta...

Agradecimientos

Gracias a mi asesor, el Dr. Joel Jones, por las enseñanzas de todos estos años, desde que ingresé a la facultad. Agradezco la confianza y el apoyo constante durante estos últimos meses, han sido fundamentales para el desarrollo de esta tesis y, aún más importante, para mi crecimiento profesional.

Gracias al Grupo de Altas Energías PUCP por las tantas oportunidades de aprendizaje.

Y gracias a mi madre, por seguir empujando día y noche.

This work was done with the financial support of Pro CIENCIA, CONCYTEC (Peru's National Council for Science and Technology), Contract 123-2020-FONDECYT

Contents

List of Figures	vi
List of Tables	vii
1 Introduction	1
2 The Standard Model and beyond	3
3 The Large Hadron Collider	10
3.1 The ATLAS Experiment	12
3.2 Sub detectors	13
3.2.1 The Inner Detector	13
3.2.2 Calorimetry	13
3.2.3 The Muon System	20
4 The ATLAS search for LLPs with the CalRatio trigger	22
4.1 Overview	22
4.2 The Model	24
4.3 Implementation	26
4.3.1 The PUCP Toy Detector	26
4.3.2 Simulation of calorimeters	34
4.3.3 Triggers and Selection	37

4.3.4	Event selection	39
4.3.5	Background estimation	41
4.4	Results	42
5 Summary and Conclusions		48
Bibliography		50

List of Figures

3.1	ATLAS detector	12
3.2	ATLAS ID efficiency	14
3.3	Bethe Bloch graph	15
3.4	ATLAS ECal barrel geometry	18
3.5	ATLAS ECal resolution	19
3.6	ATLAS Muon System efficiency	21
4.1	Feynman diagram for a dark pion model	25
4.2	Main program flow chart	28
4.3	PUCP Toy Detector flow chart	29
4.4	Geant4 simulation of particles through a block of steel for ATLAS HCal barrel . .	36

List of Tables

2.1	Gauge quantum numbers of the fermionic fields	5
3.1	Dimensions of the ATLAS sub detectors	12
3.2	Properties of calorimeter materials	20
4.1	Tag assigned to each sub detector	30
4.2	CalRatio Trigger	37
4.3	High Level Trigger	40
4.4	Event selection restrictions	41
4.5	Combination of masses of the scalar and the LLP, and $c\tau$ reported in [2]	42
4.6	Results model: $m_\Phi = 1000$ GeV and $m_{\pi_d} = 275$ GeV	46
4.7	Results model: $m_\Phi = 600$ GeV and $m_{\pi_d} = 150$ GeV	46
4.8	Results model: $m_\Phi = 400$ GeV and $m_{\pi_d} = 100$ GeV	46
4.9	Results model: $m_\Phi = 200$ GeV and $m_{\pi_d} = 50$ GeV	47
4.10	Results model: $m_\Phi = 125$ GeV and $m_{\pi_d} = 55$ GeV	47
4.11	Results model: $m_\Phi = 60$ GeV and $m_{\pi_d} = 5$ GeV	47

Chapter 1

Introduction

The SM provides a description of all the elementary particles and establishes the principles of their interactions. The model contains 12 fermions with spin $\frac{1}{2}$, four bosons with spin 1, and a fifth boson with spin 0. The fermions are divided in quarks and leptons. There are 6 quarks: up (u), charm (c), top (t), down (d), strange (s) and bottom (b), the first three with charge $\frac{2}{3}$, and the following with charge $-\frac{1}{3}$, all quarks carry colour charge; and 6 leptons: electron (e^-), muon (μ^-), tau (τ^-), electron neutrino (ν_e), muon neutrino (ν_μ) and tau neutrino (ν_τ), the first three with charge -1, and the following with no charge. The four spin 1 bosons are the force mediators, the photon (γ) mediates the electromagnetic interactions, the gluon (g) the strong interactions and the W^\pm and Z^0 bosons mediate the weak interactions. The spin 0 boson generates the mass of all the particles by the Brout-Englert-Higgs Mechanism, it is known as the Higgs boson. Quarks can interact via the three forces while charged fermions interact via the weak and electromagnetic force, and the neutrinos only with the weak force.

The particle content of the SM has been entirely verified and its predictions have been experimentally successful. However, it is not complete. The SM presents several problems such as the lack of neutrino masses: it defines neutrinos as massless, on the contrary, it has been observed that neutrinos have small masses by measuring neutrino oscillations. Moreover, it has a hierarchy problem related to the difference in magnitude between the small Higgs boson mass and the Planck

scale.

Extensions to the SM trying to solve these problems are called beyond the SM (BSM) models. One solution to the neutrino mass problem is the Seesaw mechanism. This mechanism adds new heavy SM singlets coupling to the Higgs boson giving mass to the neutrinos through mixing. A possible solution to the hierarchy problem is the theory of Supersymmetry (SUSY), which assigns to every SM particle a SUSY partner with different spin. [1]

The two possible solutions mentioned above have regions of the parameter space where particles with long lifetimes can exist. These particles are called long lived particles (LLPs) and are characterized by being able to move a macroscopic distance before decaying. The LLPs have not yet been thoroughly searched for. In this thesis we will focus on a search for these type of particles done using a specific trigger called the CalRatio trigger in the ATLAS experiment.

This document is divided as follows: Chapter 2 outlines the ingredients of the Standard Model and presents the Seesaw mechanism as a possible BSM model, in Chapter 3 we present the Large Hadron Collider and all the relevant features of the ATLAS detector. In Chapter 4 we present the recast and validation of a search for LLPs using the CalRatio trigger in the ATLAS experiment. For this, we introduce the PUCP Toy Detector and discuss the implementation for the validation, presenting the model used, the CalRatio trigger, the selection cuts and the results obtained. Finally, in Chapter 5 we summarize and conclude.

Chapter 2

The Standard Model and beyond

The Standard Model (SM) of particle physics describes the composition of matter by unifying three of the four fundamental forces through an elegant framework of gauge symmetry. This Chapter develops the theoretical foundations of this theory, emphasizes the problems the SM has, and describes possible solutions leading to LLPs.

At the center of the SM relies the concept of local gauge symmetry. This principle entails that the laws of physics should remain invariant under certain transformations performed at each point in space and time. The field $\psi(x)$ should be invariant under a transformation similar to:

$$\psi(x) \rightarrow e^{i\alpha(x)}\psi(x).$$

These transformations are characterized by Lie groups, mathematical structures that contain symmetries of physical systems. Gauge theories, such as Quantum Electrodynamics (QED), Quantum Chromodynamics (QCD), and the electroweak theory, use local gauge symmetries to describe the interactions of particles. The symmetries of the SM are:

$$SU_C(3) \otimes SU_L(2) \otimes U_Y(1) \tag{2.1}$$

The existence of these symmetries imply the appearance of gauge bosons: gluon (g), coming

from the $SU_C(3)$ symmetry (C from color), W_μ^1, W_μ^2 and W_μ^3 , product of the $SU_L(2)$ symmetry (L from “left handed”, discussed later), and B_μ coming from the $U_Y(1)$ symmetry (Y from hypercharge). The last four bosons mix, through a process called electroweak symmetry breaking (EWSB) produced by the Higgs boson, to form the observable force carriers bosons through:

$$A_\mu = \frac{gB_\mu + g'W_\mu^3}{\sqrt{g^2 + g'^2}} \quad (2.2)$$

$$Z_\mu = \frac{-g'B_\mu + gW_\mu^3}{\sqrt{g^2 + g'^2}} \quad (2.3)$$

$$W_\mu^\pm = \frac{W_\mu^1 \pm iW_\mu^2}{\sqrt{2}} \quad (2.4)$$

where A_μ represents the photon, carrying the electromagnetic force, and Z_μ and W_μ^\pm carry the weak force, the first one in charge for the neutral currents and the last one for the charged currents. Bosons before the symmetry breaking represent interaction eigenstates and bosons after it represent the mass eigenstates. The g and g' represent the couplings of the $W_\mu^{1,2,3}$ and the B_μ bosons respectively.

The particle content of the Standard Model also involves fermions, elementary particles with half integer spin. These fermions are organized into two categories: quarks and leptons, with each category further divided into three generations. Quarks, carrying fractional electric charges and color charges, form color neutral hadrons through the strong force mediated by gluons. Leptons constitute another essential category within the SM. These particles are categorized into three generations, each comprising an electrical charged lepton (charge -1) and its corresponding, chargeless and massless neutrino. The above particles and their properties are described by Weyl spinors with specific transformations under the SM symmetries in Eq. 2.1.

There are three symmetries in nature: charge conjugation (C), parity transformation (P) and time (T). The SM conserves the whole CPT symmetry, but is allowed to violate one or two of them. The SM is a chiral theory, which means, under the invariance of P symmetry, it leads to the definition of right handed and left handed particles. In Table 2.1 we show the gauge quantum numbers for each field of the SM that lead to the electric charge Q in the Gell-Mann-Nishijima

relation:

$$Q = T_3 + \frac{Y}{2}, \quad (2.5)$$

where T_3 is the third component of isospin and Q the electric charge. In the table, Q_L^i represents the quark left handed doublets, $(u^c)_L^i$ and $(d^c)_L^i$ the right handed anti-quark singlets, L_L^i the leptons left handed doublets and $(e^c)_L^i$ the right handed charged anti-leptons singlets. Notice Q_L and L_L can be written as:

$$Q_L = \begin{pmatrix} u_L \\ d_L \end{pmatrix} \quad \text{and} \quad L_L = \begin{pmatrix} \nu_L \\ e_L \end{pmatrix},$$

we are showing left handed fermions, but the equivalence for right handed leptons is given by

$$(\psi^c)_L = (\psi_R)^c,$$

and there are no right handed neutral lepton singlets.

Field	$SU(3)$	$SU_L(2)$	$U_Y(1)$
Q_L^i	3	2	$+\frac{1}{3}$
$(u^c)_L^i$	3	1	$-\frac{4}{3}$
$(d^c)_L^i$	3	1	$+\frac{2}{3}$
L_L^i	1	2	-1
$(e^c)_L^i$	1	1	+2

Table 2.1: Gauge quantum numbers of the fermionic fields. [3]

The generation of mass for particles in the SM is described by the Brout-Englert-Higgs mechanism. The Higgs field is a complex scalar field transforming as a doublet under the $SU(2)$ group with the form

$$\phi = \frac{1}{\sqrt{2}} \begin{pmatrix} \phi^+ \\ \phi^0 \end{pmatrix}.$$

The potential of the Higgs boson has the form of:

$$V(\phi) = \mu^2 \phi^\dagger \phi + \lambda (\phi^\dagger \phi)^2 \quad (2.6)$$

where $\mu^2 < 0$ and $\lambda > 0$. From this we can conclude that the minimum of the potential is not in $\phi = 0$. If we replace the values of ϕ^+ and ϕ^0 on the potential, we find out that the minimum is given by $|\phi^+|^2 + |\phi^0|^2 = v^2$ where $v^2 = -\frac{\mu^2}{\lambda}$. We chose to set ϕ^+ to zero, in that way we are able to set the the Higgs doublet at its minimum to

$$\phi = \frac{1}{\sqrt{2}} \begin{pmatrix} 0 \\ v \end{pmatrix},$$

where v is the already defined vacuum expectation value (vev). This leads to the breakdown of the $SU_L(2) \otimes U_Y(1)$ symmetry (EWSB) and the generation of masses for the W and Z bosons. The $U_Q(1)$ symmetry generated by the electric charge operator remains invariant, and, as consequence, the photon does not acquire mass. The Lagrangian including only the Higgs interactions is given by:

$$\mathcal{L}_{Higgs} = \left| \left(\partial_\mu - i \frac{g}{2} \vec{\tau} \cdot \vec{W}_\mu - i g' \frac{Y}{2} B_\mu \right) \phi \right|^2 - V(\phi) \quad (2.7)$$

The first term involves the kinetic term and the interactions of the Higgs with the other gauge bosons. It is possible to see the interactions between the $W_\mu^{1,2,3}$ and B_μ bosons with the Higgs that, after the EWSB and replacing the Higgs field for its vev, the masses of the W bosons ($M_W = \frac{vg}{2}$) and Z boson are generated ($M_Z = \frac{v\sqrt{g^2+g'^2}}{2}$), as well as the mass of the Higgs ($M_H = \sqrt{2\lambda v^2}$). This symmetry breaking also imparts mass to the fermions via their Yukawa interactions with the Higgs field described by the Lagrangian:

$$-\mathcal{L}_{Yukawa} = \left((Y_u)^{ab} \bar{q}_{aL} \tilde{\phi} u_{bR} + (Y_d)^{ab} \bar{q}_{aL} \phi d_{bR} + (Y_l)^{ab} \bar{\psi}_{aL} \phi l_{bR} \right), \quad (2.8)$$

where, in all terms, there is a summation over a and b . The discovery of the Higgs boson at CERN's Large Hadron Collider in 2012 confirmed the existence of this vital missing piece and validated the Standard Model's predictions.

The sector of the SM of particle physics describing leptons is given by the following La-

grangian:

$$\begin{aligned}
\mathcal{L} = & -\frac{1}{4}\bar{W}_{\mu\nu} \cdot \bar{W}^{\mu\nu} - \frac{1}{4}B_{\mu\nu}B^{\mu\nu} \\
& + \bar{L}\gamma^\mu \left(i\partial_\mu - \frac{g}{2}\bar{\tau} \cdot \bar{W}_\mu - g'\frac{Y}{2}B_\mu \right) L + \bar{R}\gamma^\mu \left(i\partial_\mu - g'\frac{Y}{2}B_\mu \right) R \\
& + \mathcal{L}_{Higgs} + \mathcal{L}_{Yukawa} \quad (2.9)
\end{aligned}$$

where the first two terms, shown before the EWSB, will generate the W_μ^\pm , Z_μ and A_μ kinetic energies and self interactions, the following two terms involve the lepton and quark (L , R doublets) kinetic energies and interactions with the bosons already mentioned. These terms include $\bar{\tau}$ which represents the Pauli matrices and γ^μ which are the anticommuting Dirac matrices. The next terms are the ones involving the Higgs and Yukawa couplings discussed before. [4]

As seen, the SM is a very precise theory but it also faces its own challenges and open questions. One of the principal enigmas is the existence of neutrino masses. Neutrino oscillations have confirmed the existence of them, we now should understand the mechanism by which the mass is obtained. With this objective, the Seesaw Mechanism, which we will further discuss, is proposed. Another of the most compelling enigmas is the hierarchy problem, which concerns the discrepancy between the strength of the weak force and the extreme weakness of the gravitational force. The unnaturally precise fine tuning required to maintain the mass of the Higgs boson at a manageable level raises questions about the underlying framework's completeness and potential extensions. Solutions to this problem come with theories beyond the SM, as Supersymmetry.

For analyzing the enigma of the neutrino masses we need to discuss the existence of right handed neutrinos. As P symmetry is broken, we are able to differentiate left handed from right handed particles. There are no right handed neutrinos in the SM as they would not be able to interact with matter, and they had also not yet been detected. Even with the Yukawa couplings defined before, neutrinos remain theoretically massless as there is no right handed neutrino. But, as mentioned before, there is experimental evidence (neutrino oscillations) that neutrinos must have mass. A solution to this is to add by hand a right handed neutrino. This will allow a new Dirac

mass term of the form:

$$\mathcal{L}_{Dirac}^{new} = (Y_\nu)_{mn} (\bar{L}_L)_m \tilde{\phi} (\nu_R)_n + h.c. \quad (2.10)$$

where Y_ν is a new Yukawa matrix and ν_R is the new right handed neutrino (also known as sterile neutrino). This new particle must be a SU(2) singlet with electrical charge zero, which would lead us to conclude that its hypercharge (Y) is again zero by using the Gell-Mann-Nishijama relation shown in Eq. 2.5, so this neutrino would not participate in the weak interaction.

There is another solution that would imply assuming that the neutrinos follow the Majorana equation, which implies the fermion involved satisfies: $\psi^C = C\bar{\psi}^T$. The Majorana mass term that would be added to the Lagrangian would have the form of:

$$\mathcal{L}_{Majorana}^{new} = \frac{M}{2} (\bar{\nu}_R^c \nu_R + \bar{\nu}_R \nu_R^c). \quad (2.11)$$

This term violates lepton number. For this reason, and because of the presence of charged leptons in the $SU_L(2)$ doublet, this Lagrangian is not valid for SM left handed ν_s .

The simplest theory that can explain the small neutrino masses is probably the Type I Seesaw Mechanism, in which it is possible to add n new singlets representing right handed neutrinos (ν_R). The new Lagrangian would be modified to:

$$\mathcal{L}_{Seesaw} = \mathcal{L}_{SM} - \bar{L}_a Y^{ai} \tilde{\phi} \nu_{Ri} - \frac{1}{2} \bar{\nu}_{Ri}^c M_{\nu_R}^{ij} \nu_{Rj} + h.c. \quad (2.12)$$

where Y is the Yukawa matrix, M_{ν_R} a mass matrix, the a index represents e, μ and τ , and the i and j indices represent the n new added right handed neutrinos. We can choose, as an example, a mass matrix that considers only one right handed neutrino and one light neutrino:

$$M_\nu = \begin{pmatrix} 0 & m_D \\ m_D & M_{\nu_R} \end{pmatrix}.$$

This can become more complex when considering all the three light neutrinos and adding more

right handed neutrinos. [5, 6]

Diagonalizing this matrix, we are able to obtain two masses for the neutrinos, one for the SM ν and one for the new heavy ν :

$$m_{\nu}^{light} = -\frac{m_D^2}{M_{\nu R}}, \quad (2.13)$$

$$m_{\nu}^{heavy} = M + \frac{m_D^2}{M_{\nu R}}, \quad (2.14)$$

and the two new eigenstates will be:

$$|\nu_{light}\rangle = |\nu_L\rangle - \frac{m_D}{M_{\nu R}}|\nu_R\rangle \quad (2.15)$$

$$|\nu_{heavy}\rangle = \frac{m_D}{M_{\nu R}}|\nu_L\rangle + |\nu_R\rangle \quad (2.16)$$

This is a remarkable result since it shows the existence of light neutrinos with a predominant component of the SM left handed neutrino, and the existence of a heavy neutrino with a predominant component of the right handed neutrino, which would generate a not significant interaction with the SM, consistent with the experimental results.

As the interaction between the SM and the new heavy neutrino is small, given the results before, the mixing and the Yukawa coupling will also be very small. This would lead us to a small width and therefore a long lifetime. In this example we had a one ν_R Seesaw, in which we are able to fix the mass obtaining a mixing, a value for the width and the lifetime of ν_R . In the case we study a two (or more) ν_R Seesaw, we have the flexibility to vary the mixing, therefore we can define a larger part of the parameter space in which the ν_{RS} will become the LLP and would be available for probing in colliders.

Chapter 3

The Large Hadron Collider

The Large Hadron Collider (LHC) is a particle accelerator at European Organization for Nuclear Research (CERN). The principal objective is to discover and probe the mechanism for electroweak symmetry breaking, but it also studies theories beyond the SM (BSM) such as Super Symmetry, dark matter, composite Higgs models, extra dimensions and new massive gauge bosons. It operates by accelerating two beams of protons and making them collide at extremely high energies. The very large circumference (about 27 kilometers) is important for generating a collision at the required energies. The LHC works with bunches of about 10^{11} protons. These bunches are emitted every 25 ns, meaning that the frequency of collision is 40 MHz ($\frac{1}{25}$ ns $^{-1}$). Considering that the inelastic proton-proton cross section is $\sigma_{pp} = 10$ mb and the transverse area of the beam line is $\sigma_{beam} = (10\mu\text{m})^2$, then the total rate of collision is given by

$$\text{Rate}_{\text{tot}} = \left(10^{11} \frac{\text{protons}}{\text{bunch}}\right)^2 \times \frac{10 \text{ mb}}{(10 \mu\text{m})^2} \times 40 \text{ MHz} = 4 \text{ GHz} \quad (3.1)$$

The most recent information from the LHC is collected from Run 2. The center of mass energy at this run is $\sqrt{s} = 13$ TeV and the integrated luminosity $\mathcal{L} = 189.3 \text{ fb}^{-1}$.¹

Important variables reconstructed in collider physics that are going to be mentioned within this

¹The barn (b) is the unit for scattering cross section. A barn is equivalent to 10^{-28} m. The luminosity is defined as the collision rate, and hence, the unit that is used to measure it is the b^{-1} .

work are:

- transverse momentum, which is the momentum in x and y (coordinates perpendicular to the beam line) as $\vec{p}_T = (p_x, p_y)$;
- pseudorapidity:

$$\eta = \ln \left(\cot \left(\frac{\theta}{2} \right) \right), \quad (3.2)$$

where θ is the angle between the total momentum vector (\vec{p}) and its projection on the beam line (p_z);

- azimuthal angle: $\phi = \arctan \left(\frac{p_x}{p_y} \right)$;
- the angular separation of two particles: $\Delta R = \sqrt{(\Delta\eta)^2 + (\Delta\phi)^2}$;
- the momentum that is not detected:

$$\left(\vec{p}_T^{miss} = - \sum_{visible} p_T \right), \quad (3.3)$$

called missing transverse momentum. [7]

The amount of information generated by a collision of two proton beams is overwhelming and can not all be stored at once. There is a first step of hardware particle selection where the particle must have certain characteristics for the event to be recorded, on the contrary, the information of the event is discarded. This first hardware based trigger is called Level 1 (L1). Then, the data obtained passes through a second selection that is called High Level Trigger (HLT), a software trigger customized by the user.

There are currently four experiments functioning in the LHC: A Toroidal LHC ApparatuS (ATLAS), Compact Muon Solenoid (CMS), A Large Ion Collider Experiment (Alice) and LHCb. This work is focused on the ATLAS experiment [8].

3.1 The ATLAS Experiment².

The ATLAS detector is designed to study fundamental particles and their interactions, produced by proton-proton collisions with aims to study the Higgs bosons and discover particles beyond the SM. The detector (Figure 3.1) is mainly composed by four sub detectors: the Inner Detector (ID), the Electromagnetic Calorimeter (ECal), the Hadronic Calorimeter (HCal), and the Muon System (MS). We can approximate the geometry of each of these sub detectors as cylinders with dimensions given in Table 3.1, where R represents the radius of the cylinder and Z the half length.

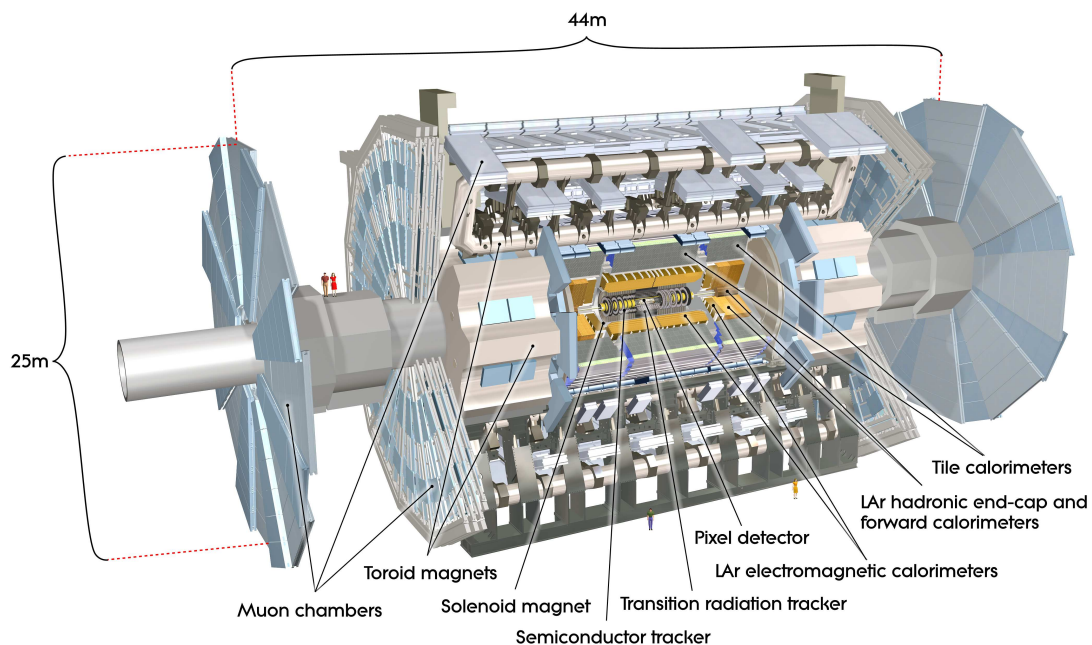


Figure 3.1: Image of the ATLAS detector.

Sub Detector	R_{min} [m]	R_{max} [m]	Z_{min} [m]	Z_{max} [m]
ID	-	1.150	-	3.512
ECal	1.500	1.970	3.512	3.830
HCal	2.280	4.250	3.830	5.500
MS	4.250	5.000	5.500	8.000

Table 3.1: Dimensions of the ATLAS sub detectors.

²All the information and figures about the ATLAS experiment in this section, unless specified, are extracted from [8]

3.2 Sub detectors

3.2.1 The Inner Detector

The ID is designed to measure the trajectories of charged particles product of a proton-proton collision. These particles leave tracks in the ID, which can further be matched to a signal in another sub detector and give a finer precision in the measurement of their properties. At intervals of 25 ns, the ID receives the product of 2×10^{11} protons colliding, therefore it is designed to have a quick response to be able to properly identify their trajectories and assign them to the correct bunch crossing.

The ATLAS ID is composed by pixel and silicon microstrip (SCT) trackers, used along with the straw tubes of the Transition Radiation Tracker (TRT). It covers an area of diameter 2.3 m and length approximately 7 m around the nominal IP. The pseudorapidity coverage is $|\eta| < 2.5$. In Figure 3.2 is shown the track reconstruction efficiency for muons, pions and electrons with $p_T = 5$ GeV (left) and for different momenta of pions (right) both in function of the absolute value of pseudorapidity. We only consider efficiencies when talking about reconstruction of tracks. In Chapter 4 we explain the implementation of this, assuming right panel for all hadrons.

The energy resolution of this tracker is given by:

$$\left(\frac{\sigma}{p_T}\right)^2 = (0.05\%p_T)^2 + (1\%)^2. \quad (3.4)$$

3.2.2 Calorimetry

The calorimeters are a type of detectors designed to measure the energy coming from an incident particle by absorbing it and generating a cascade of particles. The cascade can be electromagnetic or hadronic. A calorimeter that generates cascades of electromagnetic particles is called a “Electromagnetic calorimeter” (ECal) and one that generates a hadronic cascade is called a “Hadronic

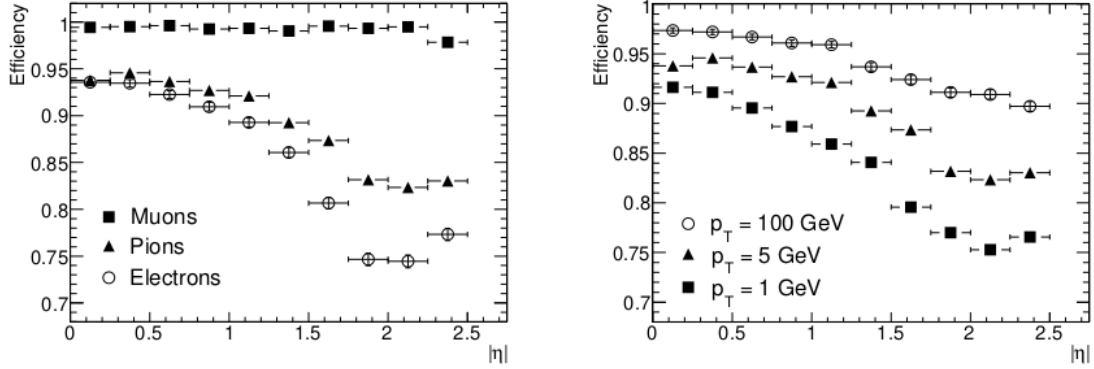


Figure 3.2: Track reconstruction efficiency of muons, pions and electrons of $p_T = 5$ GeV in function of $|\eta|$ (left). Track reconstruction efficiency for pions with $p_T = 1$ GeV, $p_T = 5$ GeV and $p_T = 100$ GeV in function of $|\eta|$ (right).

calorimeter” (HCal). The ECal is expected to stop completely electrons and photons, and absorb all their energy, while the HCal is expected to do the same with all hadrons. There are two principal types of calorimeters:

- homogeneous calorimeters: are the ones where the absorbing and detecting material is the same. This means that all the deposited energy is detected. Usually this configuration is found in the electromagnetic calorimeters.
- Sampling calorimeters: they combine layers of two different materials, a passive and an active material. The first one, also called the absorber, has the function of absorbing the energy of the particle, is commonly a heavy material; the second one is designed to generate the signal (shower of particles). These calorimeters strongly reduce costs of material and construction, but have the disadvantage that not all energy is detected. Usually hadronic calorimeters have this configuration.

Particles lose energy through different processes. For example, charged particles are involved in processes as: ionisation, excitation, Bremsstrahlung scattering or Cherenkov effect; photons are involved in photoelectric effect, Compton scattering or pair production; and hadrons are involved in nuclear interactions. We measure the energy losses in these processes as the “stopping power” (dE/dx).

The stopping power of heavy charged particles, that is, particles with masses bigger than the mass of the electron, is obtained by the Bethe Bloch formula:

$$-\left\langle \frac{dE}{dx} \right\rangle = K z^2 \frac{Z}{A} \frac{1}{\beta^2} \left[\frac{1}{2} \ln \frac{2m_e c^2 \beta^2 \gamma^2 T_{max}}{I^2} - \beta^2 - \frac{\delta(\beta\gamma)}{2} \right] \quad (3.5)$$

in which: $K = 4\pi N_A r_e^2 m_e c^2 = 0.307 \text{ MeV g}^{-1} \text{ cm}^2$ with $N_A = 6.022 \times 10^{23}$ the Avogadro number, $r_e = 2.8 \text{ fm}$ the classical electron radius, $m_e = 511 \text{ keV}$ the electron mass and $c = 3 \times 10^8 \text{ m/s}$ the speed of light. Furthermore, z is the charge of the incident particle, Z and A are the charge number and atomic mass of the medium, β is the velocity of the incident particle with respect to the speed of light, γ is the Lorentz factor, I is the mean excitation energy of the medium, δ is a density correction and

$$T_{max} = \frac{2m_e c^2 \beta^2 \gamma^2}{1 + 2\gamma m_e/M + (m_e/M)^2}$$

is the maximum transferable kinetic energy with M being the mass of the incident particle. In Figure 3.3 an example of the mean energy loss by Bethe Bloch equation is shown for different materials with respect to the particle momentum.

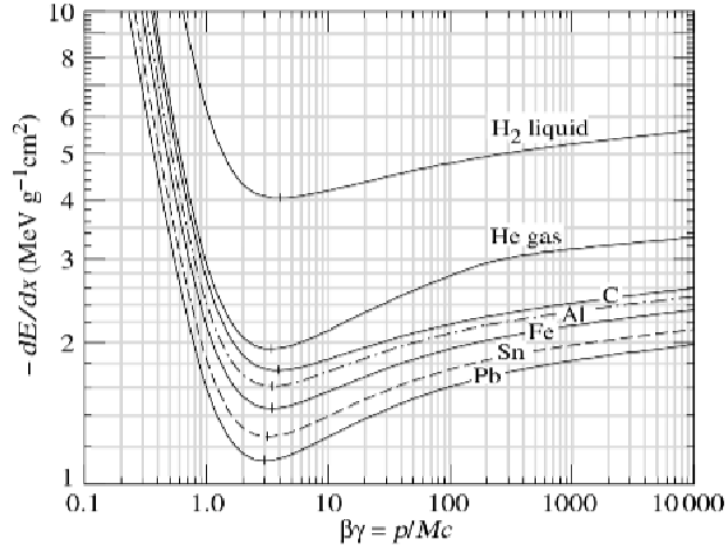


Figure 3.3: Mean energy loss for different materials. Graph obtained from [9].

The stopping power for electrons becomes predominantly Bremsstrahlung interactions and it is

given by

$$-\frac{dE}{dx}\Big|_{Brems} = \frac{1}{X_0}E \quad (3.6)$$

where X_0 is the radiation length of the material. [10] The radiation length is the distance an electron can travel inside a material losing $1/e$ of its energy through Bremsstrahlung. The X_0 changes with the material. For a block of different materials we can obtain the total X_0 by:

$$\frac{1}{X_0} = \sum_i \frac{V_i}{X_i} \quad (3.7)$$

where the index i defines the material, V_i is the volume fraction of the material i and X_i is its radiation length in distance magnitude.

Some other concepts that are interesting to discuss are: [11]

- The amount of particles in an electromagnetic shower increases until each one reduces its energy to a critical energy E_c , after that, the energy loss from ionisation and excitation becomes predominant. At that moment, the number of particles in the shower is reduced until all are absorbed inside the calorimeter. [10]
- The variable that characterize a hadron shower is the nuclear interaction length (λ_{int}). This corresponds to the average distance traveled by a hadron in a medium before a nuclear interaction happens, similar to X_0 for electromagnetic showers. The probability of a particle to travel a distance x is given by:

$$P = e^{-(x/\lambda_{int})}$$

- The Moliere Radius (ρ_M): is the radius that describes the transversal evolution of an electromagnetic shower. This depends on X_0 and E_c . This radius contains almost the complete particles shower (between 85 to 90 %).

3.2.2.1 Electromagnetic Calorimeters

The ECal generates a cascade of electromagnetic interactions whenever a particle travels through it. The cascade consists on a shower of particles that release energy proportional to the energy of the incident one. In this way the ECal absorbs the poriginal article and measures its energy. [12, 1]

The ATLAS ECal, also called the lAr calorimeter, is characterized by its accordion geometry. The barrel is composed by two halves, one covering the area of $z > 0$ ($0 < \eta < 1.475$) and the other $z < 0$ ($-1.475 < \eta < 0$). Each half barrel weighs approximately 57 tonnes. Its total length is approximately 3.2 m, its inner diameter is 2.8 m and the outer one is 4 m. The absorbers are presented in accordion geometry as can be seen in Figure 3.4 and are composed of lead plates. Each plate has a thickness of 1.53 mm for $|\eta| < 0.8$, and 1.113 mm for the rest. Each plate is covered by a 0.2 mm thick stainless steel sheet (properties of all the calorimeter materials can be found in Table 3.2). From all this information we can calculate the abundance of lead in the calorimeter, which is around 79%.

In the inner radius of the ECal we find a liquid argon layer called presampler, which is 11 mm in depth and covers all the pseudorapidity range. It generates a shower sampling before the particles enter the active medium.

The end caps cover a range of pseudorapidity between 1.375 and 3.2. They are composed by two wheels on each side of the detector. Each wheel is 63 cm thick and weights 27 tonnes. Both are also composed by lead plates working as absorbers, in this case they have a thickness of 1.7 mm for $|\eta| < 2.5$ and 2.2 mm for $|\eta| > 2.5$. The total thickness of each wheel varies from $24 X_0$ to $38 X_0$. There is also a lAr presampler that covers $1.5 < |\eta| < 1.8$ to improve the measurements.

The energy resolution of an ECal is parametrized by

$$\left(\frac{\sigma}{E}\right)^2 = \left(\frac{S}{\sqrt{E}}\right)^2 + \left(\frac{N}{E}\right)^2 + C^2 \quad (3.8)$$

where S is the stochastic term, N the noise term which comes from the electronics, and C is a constant. The stochastic term has a value of 10.1% and the constant of 0.17%. The noise term is

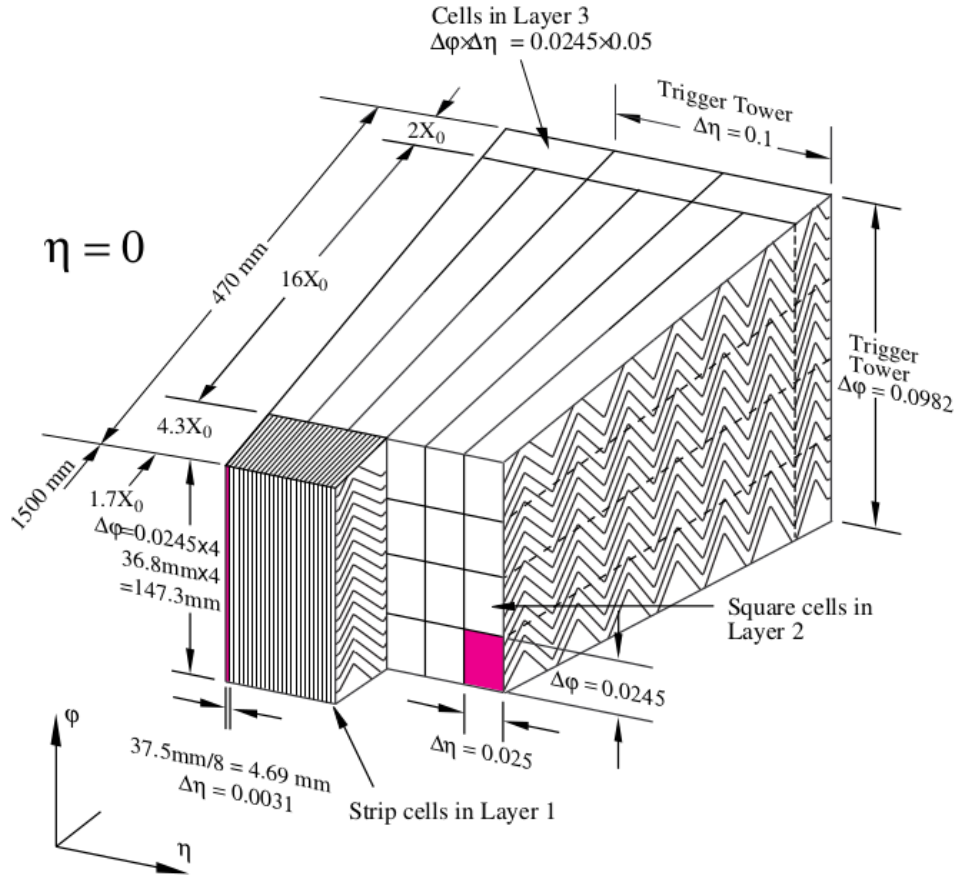


Figure 3.4: ATLAS ECal barrel geometry.

not considered. In Figure 3.5 we show this function considering the values given for this specific calorimeter.

3.2.2.2 Hadronic Calorimeters

The HCal is in charge of absorbing and measuring the energy of all hadrons coming from the proton-proton collision. Similarly to the ECal, in the ATLAS HCal, the barrel, also called the tile calorimeter, covers $|\eta| < 1.7$ and the end caps cover the range until $|\eta| = 3.2$.

The tile calorimeter is a sampling calorimeter that uses steel as the absorber and scintillator as the active medium. It has a central barrel of length 5.8 m and two external barrels each of 2.6 m length. The three of them with inner radius 2.28 m and outer radius 4.25 m and with a depth of approximately 7.4 nuclear interaction lengths (λ_{int}). The ratio of material between steel and

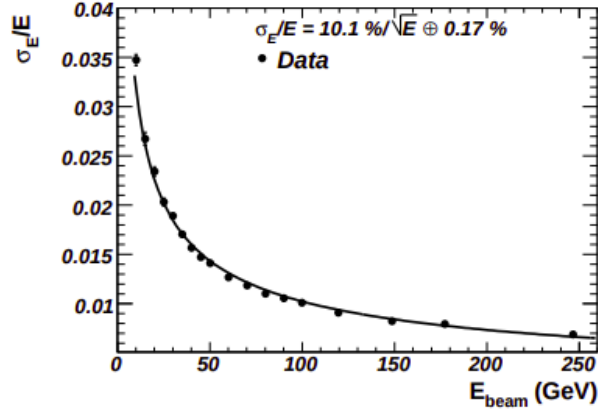


Figure 3.5: ATLAS ECal percentage energy resolution function of energy.

scintillator is about 4.7:1, which makes the abundance of steel approximately 82%. For simplicity, we set the component of this detector to 100% steel (see Section 4 for discussion on the simulations).

The end caps of this HCal are also sampling calorimeters, they are made of liquid Argon and copper, and cover a range of $1.5 < |\eta| < 3.2$. Each end caps are two wheels of outer radius of 2.03 m. The inner wheels are composed of 24 copper plates of 25 mm thickness each with addition of a front plate of 12.5 mm. The second wheel has 16 copper plates of 50 mm thickness each and a front plate of 25 mm. Between the plates there are gaps of 8.5 mm with 4 layers inside of lAr of 1.8 mm each. This lead us to conclude that each end cap has a thickness of 1.786 m from which 1437.5 mm are copper and 295.2 mm lAr. Copper is going to be about 83% of the whole calorimeter.

The resolution of this calorimeter is also given by Equation 3.8, for the tile calorimeter the parameters are: $S = (56.4 \pm 0.4)\%$ and $C = (5.5 \pm 0.1)\%$, there is no noise term reported. Similarly for the end caps, the parameters are: $S = (21.4 \pm 0.1)\%$, C is close enough to zero to not be considered, and N is not reported.

In addition, the ATLAS calorimetry system includes also a Forward calorimeter (FCal), located outside the detector, that covers a range of $3.1 < |\eta| < 4.9$. Is designed to receive particles at a distance approximately of 4.7 m from the interaction point and is exposed to a high energy flux. This part of the calorimeter would not be taken in consideration for simulation.

Material	Z	A [g/mol]	X_0 [cm]	λ_{int}	E_c [MeV]	R_M [cm]	I [eV]
lAr	-	-	14.0	85.7	30.5	10.0	188
Copper	29	63.546	1.436	15.32	19.42	1.568	322
Zinc	30	65.38	1.742	19.42	18.93	1.952	330
Aluminum	13	26.98	8.897	39.70	42.70	4.419	166
Lead	82	207.2	0.5612	17.59	7.43	1.602	823

Table 3.2: Properties of calorimeters materials. [13, 11]

3.2.3 The Muon System

The MS has three principal functions: identifying, reconstructing and triggering signals coming from muons. The ATLAS MS covers the range of $0 < |\eta| < 2.7$. It is composed by a toroid generating a magnetic field for the deflection of muon tracks. This system is composed by chambers that identify the bunch-crossing, and measure p_T and coordinates of muons. A muon passing over any of these chambers ionizes a gas and generates an image charge that can be stored as signal.

The efficiency of this MS is given by Figure 3.6. On the left panel is shown the efficiency versus the transversal momentum for stand alone muons (only analyzed by the MS) and combined efficiency (MS + ID). On the right panel the efficiency is shown graphed over the pseudorapidity for a muon of $p_T = 100$ GeV. It is possible to observe the decrease in the efficiency around $|\eta| = 1.4$ because of the change from barrel to endcaps and also the decrease on $|\eta| = 2.5$ and 2.7 for combined and stand alone respectively, this because of the end of pseudorapidity acceptance in each sub detector.

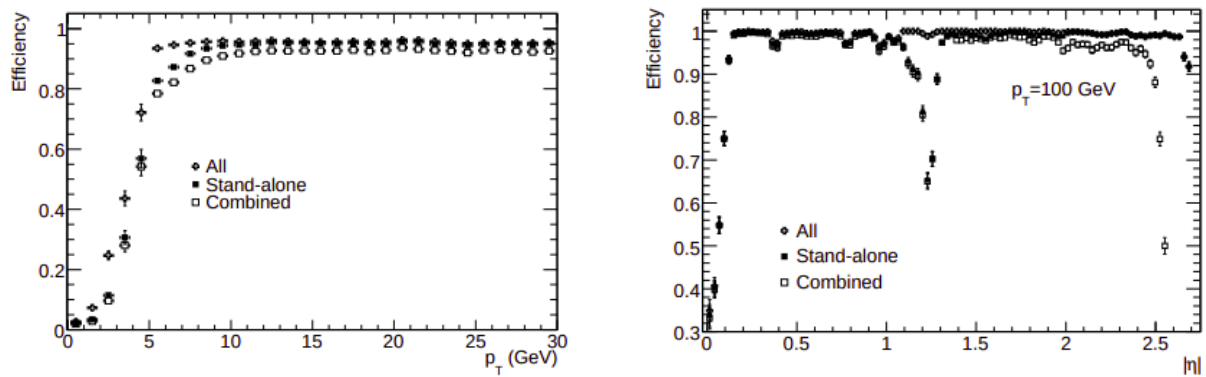


Figure 3.6: ATLAS Muon System efficiency for stand alone muons (MS only) and combined efficiency (MS + ID). Left: Efficiency versus transversal momentum. Right: Efficiency versus pseudorapidity.

Chapter 4

The ATLAS search for LLPs with the CalRatio trigger

4.1 Overview

Searching for LLPs is a way of searching for new physics in colliders. In this Chapter we will introduce some searches already done on the ATLAS and CMS experiments, describe the triggers used and the implementation done for the recast.

While searching for LLPs, two factors will determine the approach of the search: the products of the LLP decay and the mean lifetime of the LLP. The first one will determine the type of trigger used and, the second, the sub detector in which the search will take place. For instance, searches done in the muon system of both, CMS and ATLAS experiments, are triggered by displaced dimuons, specifically in models that contain a neutral LLP decaying into two muons. In [14] the CMS Collaboration searches for this type of signal in the LHC Run 1 data, with center of mass energy $\sqrt{s} = 8$ TeV in the context of two models. The first one proposes the LLPs as spinless bosons (X) pair produced from the decay of a non-SM Higgs ($H^0 \rightarrow X X$), which is produced by gluon gluon fusion. The X boson decays into two muons ($X \rightarrow \mu^+ \mu^-$) with a decay length chosen to be 20, 200 and 2000 cm. In the second model, a pair of scalar quarks (squarks \tilde{q}) is considered,

each of them decaying into a quark and a neutral fermion (neutralino $\tilde{\chi}$), the latter being the candidate for LLP, ($\tilde{q} \rightarrow q\tilde{\chi}$). The neutralino decays into two muons and a neutrino ($\tilde{\chi} \rightarrow \mu^+\mu^-\nu$) with approximately 200 cm of mean transverse decay length given by the chosen coupling¹. There is also an actualization of this search with data from a collision with center of mass $\sqrt{s} = 13$ TeV [12]. In this search two muons product of a long lived scalar boson X are coming from the decay of a BSM Higgs ($H \rightarrow X X$). This search is based on [15] and [16]. In both cases no excess over the SM background is observed. Bounds on the LLP characteristics are placed.

The ATLAS Collaboration presents a similar search for displaced dimuons in the muon chambers in [17], with center of mass energy 13 TeV. They use the Muon RoI Trigger [18], a signature driven trigger for the MS of ATLAS detector which selects isolated signal-like events and non isolated background-like events. This trigger selects events with clusters of L1 Regions of Interest (RoIs) in the MS that are isolated from activity in the ID and calorimeters. It will be effective for LLPs decaying between 3 to 7 m from the PV and having masses greater than 10 GeV. After the trigger selection, the analysis requires either two reconstructed displaced vertices in the MS or one ID vertex and one MS vertex. The combination between sub detector increases sensitivity to shorter lifetimes than an analysis only considering MS vertices could have. No excess over the SM background is observed.

Searches that include tracks in the ID have also been performed. In this type of searches standard triggers are applied for selecting events with high p_T jets or leptons, and an unusual amount of missing energy. An example can be found in [19] where a search has been performed with a benchmark model inspired by SUSY. The search presented is sensitive to models predicting events with significant missing energy, and at least one displaced vertex with five or more tracks and a visible invariant mass greater than 10 GeV. The search has not found a significant excess of events over the SM background. This type of searches are not sensible to low masses LLPs.

There had also been performed searches for displaced jets in the calorimeters. In [20] a search for LLPs decaying into displaced jets is conducted in the CMS experiment using as benchmark

¹In SUSY models, this coupling violates R-parity.

models different SUSY inspired models. A dedicated trigger is used to capture events with displaced jets signatures, discriminating jets and secondary vertices from signal produced by the SM background. The signal observed is in agreement with the SM.

Searches in the calorimeters performed by the ATLAS Collaboration can be found in [21], [22] and [2]. This work will focus on the last one. The first search is performed on data collected from proton-proton collisions at $\sqrt{s} = 8$ TeV and the last two are at $\sqrt{s} = 13$ TeV. The three of them search for LLPs decaying into jets in the outer region of the ECal or inside the HCal, for this, different versions of a CalRatio trigger are used. This trigger is specialized on recognizing such types of signals; it selects at least one trackless jet with most of its energy deposited in the HCal and only a small fraction of its energy deposited in the ECal.

In this Chapter we will introduce the Model used in [2], describe the PUCP Toy Detector and give details on we used it to reproduce the results obtained in this search for neutral LLPs decaying into hadronic jets in the calorimeter done by the ATLAS Collaboration. For this, two CalRatio triggers are used, both conformed by a Level 1 (L1) Trigger and a High Level Trigger (HLT), followed by specific cuts for the event selection process. We also comment on the Machine Learning methods used by ATLAS, as well as our procedure in front of them.

4.2 The Model

We will consider the benchmark model presented in [2] in order to validate our simulation of the CalRatio search. The search considers neutral scalar LLPs (π_d) produced from the decay of a heavy scalar field (Φ). This scalar could be interpreted as the SM Higgs Boson, but we will vary the mass to a wider range of masses. The process we simulate is shown in Figure 4.1, where the scalar field Φ is produced by gluon fusion and then decays into a pair of π_d s. This model will be simulated in MadGraph5 [23].

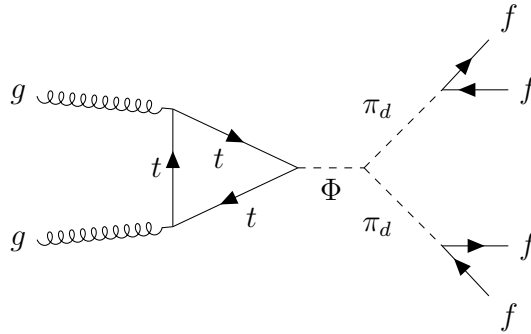


Figure 4.1: Feynman diagram for a dark pion model. A heavy scalar field Φ is produced via gluon fusion and decays into two long lived dark pions. Each of them decays into a pair of fermions generating jets.

The π_d travel a macroscopic distance before decaying entirely into SM fermions. They are assumed to have Yukawa-like couplings, similar to those of the Higgs, meaning that they decay into $b\bar{b}$, $c\bar{c}$, $\tau^-\tau^+$ in approximate ratio of 85:8:5, assuming they are heavy enough. The lifetime of the LLP is considered to be uncorrelated to its mass. The model has three free parameters: $m_\Phi \in [60, 1000]$ GeV, $m_{\pi_d} \in [5, 475]$ GeV and $c\tau_{\pi_d} \in [0.02, 10]$ m.

The SM fermions, product of the decay of the LLPs, generate jets with an origin far from the interaction point (IP) of the colliding protons. These jets are known as displaced jets and, if generated within the ID, produce displaced vertices. When the LLP decay occurs inside the calorimeters, the decay products are collimated enough in a way it is possible to be reconstructed as a single trackless jet, containing the majority of its energy deposited in the hadronic calorimeter (since the LLP decays mostly to hadrons).

The analysis done focuses on recognizing these non standard jets. The analysis by ATLAS considers two procedures for selecting particles based on the mass used for Φ in their simulation: one optimized for scalar masses over 200 GeV (*High- E_T*) and another one for masses below 200 GeV (*Low- E_T*), where E_T represents the transverse energy.

The dominant background process that best mirrors the signal is a SM multi-jet production, particularly when the jets are principally composed of neutral hadrons or when they have misreconstructed tracks. Even though the probability for a prompt jet to reproduce the characteristics

of signal-like jets is considerably low, the high cross-section of SM multi-jet events makes it the predominant background in this search. Additional contributions arise from jets reconstructed from non-collision sources, which include cosmic rays and beam-induced background (BIB).

4.3 Implementation

4.3.1 The PUCP Toy Detector

We have constructed a Toy Detector of the ATLAS experiment with the objective of searching for signals of long lived particles. It is based on C++, Pythia8 [24] and FastJet [25]. It needs to be called from a main program that receives information of a process through a Les Houches event (LHE) file [26] as an input and carries out the parton shower and hadronization using Pythia8.

In Figure 4.2 we show a flow chart of the main program. The main program calls the Toy Detector and performs a loop over all the events. Inside the loop it is possible to perform any search for LLPs, in this case we implemented the CalRatio triggers and the selection process used in [2], which will be explained later in this Section.

The Toy Detector itself receives as input a Pythia8 object per event, carrying the full information of the process, and returns the identification codes for the detected particles and the clustered jets with information of where were they detected and their reconstructed momentum, taking into account the detector efficiency.

A flow chart for the Toy Detector is shown in Figure 4.3. As mentioned before, this detector receives a Pythia8 object containing all the information of the event, meaning it contains all particles generated during the collision, with their respective characteristics (energy, momentum, pseudorapidity, phi angle, coordinates of production and decay, etc). The detector performs a loop over all particles of the event and analyzes each one separately. If it is a neutrino, an uncharged stable BSM particle, has an absolute pseudorapidity greater than the accepted by any sub detector ($|\eta| > 3.2$) or is produced outside the detector, the particle is not considered. Then, the detector assigns a special tag to the particle depending on the sub detector it is generated in, by its produc-

tion coordinates (see Table 4.1). We have two tags for the HCal since it has different materials for the barrel and for the end caps. Depending on the tag, the detector runs a different routine, each of them determining the measured momentum, energy and pseudorapidity using the corresponding efficiency and resolution of the sub detector. If the particle is detected, the reconstructed variables are saved in a vector containing all detected particles in the sub detector. We have four vectors, one for each sub detector (ID, ECal, HCal and MS). These vectors contain the information of all detected particles in a self defined class called PartDet with the form:

```
class PartDet {  
    public:  
    long int id;  
    double pt;  
    double pz;  
    double energy;  
    double mass;  
    double eta;  
    double phi;  
    double xini;  
    double yini;  
    double zini;  
    bool fromsec;  
};
```

where `id` refers to the Particle Data Group (PDG) [13] identification code of the particle, `pt` to the reconstructed transverse momentum, `pz` to the projection of the reconstructed momentum in the beam line, `energy` is the detected energy, `mass` the mass of the particle, `eta` the detected pseudorapidity, `phi` the reconstructed phi angle, `xini`, `yini` and `zini` are the coordinates where the particle first appears in the detector, and `fromsec` is a bool that turns to unity when the particle is considered a secondary particle (meaning it is produced in a shower generated inside a calorimeter)

and 0 when it is not.

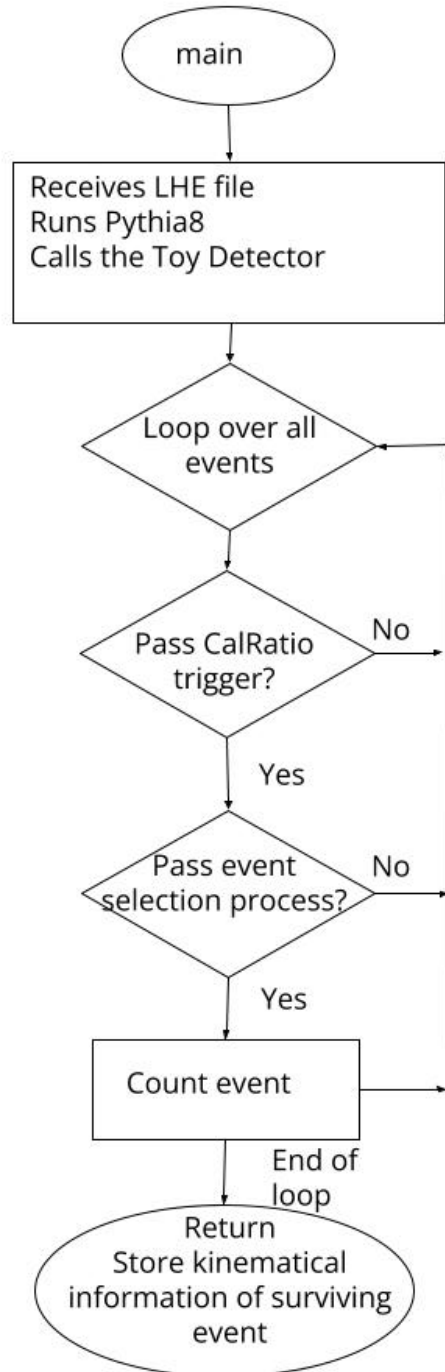


Figure 4.2: Main program flow chart.

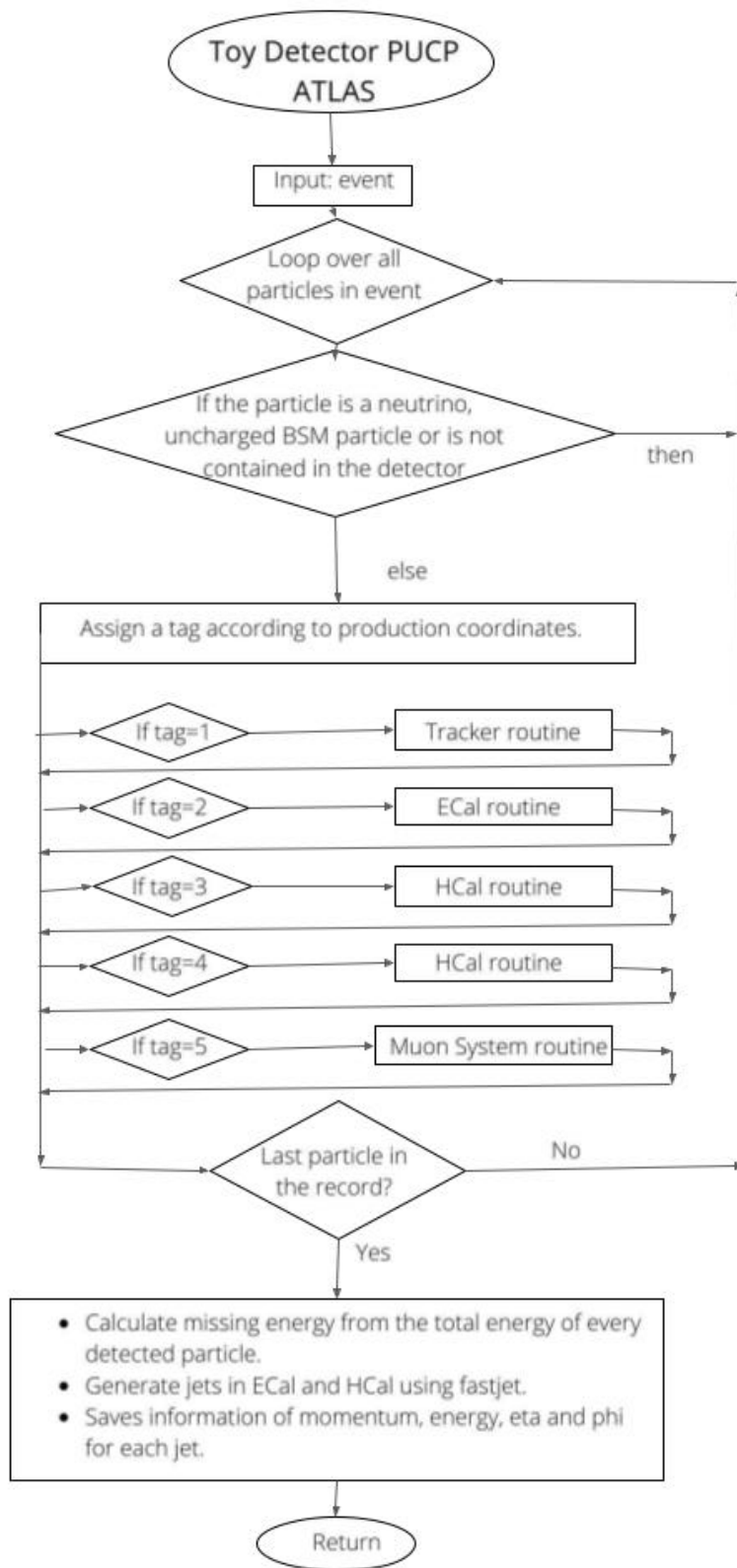


Figure 4.3: PUCP Toy Detector flow chart.

Sub Detector	Tag
ID	1
ECal	2
HCal barrel	3
HCal end caps	4
MS	5

Table 4.1: Tag assigned to each ATLAS sub detector in the PUCP Toy Detector.

The particle is then geometrically propagated to the next sub detector, unless it has been detected in the MS, and proceeds to perform the corresponding sub detector routine. The propagation is carried out using the production coordinates, pseudorapidity (η) and phi angle (ϕ). With this information we are able to determine the coordinates where the particle exits a sub detector and the coordinates when it later enters to the next one.

The routines for the calorimeters analyze also the deposited energy with a Geant4 simulation, explained in the following paragraphs, from which we are able to determine the detected energy. This simulation also returns a vector with all the secondary particles exiting the calorimeters with η and ϕ angle matching the original particle (we assign by hand the same direction of momentum of the incident particle). These particles must also be analyzed to identify if they are detected in the HCal barrel or end caps (secondaries coming from the ECal), or in the MS (secondaries coming from the HCal). For this, we developed a different routine for each sub detector that includes the same features of the original one, but is computationally designed to analyze variables from a different class, designed specifically for the secondaries. The class defined is:

```
class PartSec{
    public:
    long int id;
    double energy;
    int quant;
    double mass;
    double prodR;
```

```
double xprod;
```

```
double yprod;
```

```
double prodZ;
```

}; where `quant` describes the quantity of particles with the same `id` exiting the calorimeter, `xprod`, `yprod` and `zprod` are the production coordinates and `prodR` is the modulus of the production coordinates in the transversal plane. The routines designed for evaluating variable from this class also generate a loop in the variable `quant` so that we are able to analyze the exact amount of particles generated in the shower, each of them going through the efficiency and resolution functions.

The functions of efficiency for each sub detector routine are fits coming from the reported results of the ATLAS experiment. The efficiency of the ID is implemented for all hadrons using the data reported on the right panel of Figure 3.2. We assumed all hadrons have a similar efficiency to the one reported for pions, then we obtained a function that fits each set of data ($p_T=1$ GeV, $p_T=5$ GeV, $p_T=100$ GeV) and depends only on pseudorapidity. If the particle being analyzed is not a hadron, we assumed it is always detected and the efficiency is 1. Finally, we made a linear interpolation on the momentum for finding the efficiency corresponding to the real momentum of the analyzed particle. Similarly, in the MS we used a fit for the efficiency for stand alone muons reported in the left panel of Figure 3.6. The fit goes from momentum 0 to 7.5 GeV, then for any higher momentum we assume the efficiency is constant and close to 1. We assumed this applies for all type of particles. We do not apply this efficiency in the calorimeters.

Given the obtained value for efficiency, inside each detector sub routine we generate a random number between 0 and 1 in a uniform distribution. If the number is greater than for the efficiency, the particle is not detected and passes directly to the next sub detector, if it is lower, then the particle is detected, the information saved and passes to the next sub detector (i.e. the ECal if originally in the ID).

The functions of resolution used are given in Equation 3.4 for the ID and Equation 3.8 for the calorimeters. For the MS we assume the resolution is always 0 (meaning perfect reconstruction) unless the momentum of the particle is greater than 1 TeV, then it is 0.1. The resolution function for

any sub detector depends on the momentum, pseudorapidity and energy of the analyzed particle. We obtain the value through these equations and then generate the smearing. For this process we generate a number from a random Gauss distribution centered in zero and calculate a new detected momentum using:

$$p_T^{det} = p_T \times (1 + res \times RndmG)$$

where p_T is the initial momentum of the particle, res is the resolution obtained and $RndmG$ is the random Gauss generated number. From this new detected momentum we calculate the detected energy.

A very important feature of this work, relevant in particular to LLPs is that we also calculate a reconstructed pseudorapidity and phi angle. These variables, when given by Pythia8, are defined as Equation 3.2 with $\tan(\theta) = p_T/p_z$ and $\tan(\phi) = p_x/p_y$. Even though this geometrically helps to understand how the particle travels through the detector, it does not give any information about the position inside any sub detector, which can lead to inconsistencies at the moment of defining jets. For this, we need to redefine the variables assuming the particle is coming from the IP, such that η and ϕ now refer to regions of the detector where the particle is, rather than features of its momentum. We used the variables given by Pythia8, including the production coordinates to calculate the coordinates where the particle enters and exit a sub detector, then we use the entering coordinates to define a vector coming from the IP. From this vector we calculate the elevation angle (θ) which is going to be used to calculate the reconstructed pseudorapidity with Equation 3.2, and the ϕ angle. We used the entering coordinates as the energy deposition of a particle inside any sub detector is stronger.

At the end of the particle loop, with all the information of the reconstructed particles and momenta on each sub detector, we calculate the total missing energy of the event by subtracting all the detected momentum as shown in Equation 3.3. If a particle has been detected in the ID, the momentum that will be considered for this calculation is the one reconstructed in the ID, if it is not, the momentum considered will be the one reconstructed in both of the calorimeters.

We also generate the jet clustering for the analysis, using FastJet with R parameter 0.4. For

this we designed an algorithm that acts over all energy deposits in the ECal and HCal. It generates the clustering and defines jets with p_T over 30.0 GeV. An important requirement of the CalRatio trigger is that it will be necessary to know how much energy is deposited by the same jet in different calorimeters. For this, we made a loop inside each jet over all the constituents, if the constituent is a particle detected in the ECal, the energy detected adds to a variable, inicialized in 0, called `eneecal`, and if it is detected in the HCal, the energy is added to a similar variable called `enehcal`. We demonstrated that the sum of `eneecal` and `enehcal` is the exact total energy of the jet, as expected. For calculating the coordinates where the jet is produced, we used a weighted average by vectorially adding all the production coordinates of the constituents, each multiplied by their individual energy deposit, and then dividing it by the total amount of energy of the jet. At the end, we save the information of all the jets in a vector of a self designed class called `JetDet` of the form:

```
class JetDet {
    public:
        double pt;
        double pz;
        double energy;
        double eta;
        double phi;
        double xini;
        double yini;
        double zini;
        bool fromsec;
        double ecale;
        double hcale;
};
```

with all the present variables explained before.

4.3.2 Simulation of calorimeters

As mentioned earlier, a crucial part of the analysis is to be able to recognize the amount of energy particles deposit inside each calorimeter, and which of them continue traveling to the next sub detector. This is a not trivial problem. For solving it we developed a Geant4 [27, 28, 29] simulation of the particles traveling through the calorimeter materials.² The objective is not only to calculate the amount of energy deposited by prompt particles traveling through the whole calorimeter, but it is to to calculate the energy deposition a particle produced in the middle or latter part of the calorimeter could generate. In that way, it would travel only a percentage of the whole length, the deposition will be smaller and the shower exiting the calorimeter will be composed by a different amount of particles with different energies each. This calculation is particularly relevant for particles coming from the decay of neutral LLPs, which leave a displaced signal that will pass the CalRatio trigger.

We based this simulation on the example given in the extended hadronic Geant4 library: Hadr07. This example is designed to reproduce a hadronic sampling calorimeter with a wide amount of absorbers of different materials and thicknesses. It generates the physics of a hadronic cascade (also including electromagnetic showers) produced by the interactions between a given particle and the absorbers.

During a proton-proton collision, a large amount of particles is created. From there, we choose which relevant particles to simulate (K^+ , K^- , K_L^0 , K_S^0 , μ^+ , μ^- , Λ , n^0 , Σ^+ , Σ^- , π^+ , π^- , p^+ , γ , e^+ and e^-) by analyzing which particles lived enough inside the calorimeters to be able to deposit a relevant amount of energy.

We designed the detector geometry as a box (one absorber) of the most abundant material in each calorimeter. The dimensions of this box varied according to the real dimensions of the calorimeter, in order to be able to calculate energy depositions of particles being produced at any stage of the calorimeter. For each one (ECal, HCal barrel and HCal end caps) we used 22 different lengths, that represented the dimensions of the box, separated logarithmically from each others: starting on 1.0

²This simulation is going to be presented soon by this author as a thesis for obtaining a Degree in Physics.

mm and finishing in the longest distance a particle can travel inside the simulated calorimeter.

This simulation in Geant4 receives as input the incident particle with specific incident energy, the material of the detector that is going to be used and the length of the detector. It returns as output the deposited energy with its respective error and information of the secondary particles (particles emerging from the detector), such as type, energies, probability of emerging and average quantity of particles emerging.

For obtaining the exact energy deposition of a particle with incident energy E that travels a given distance D we generate a double linear interpolation. We select the two simulated values of travel distance that are the closest to the real value D , D_1 and D_2 (one smaller and one bigger) and we do the same for the incident energy obtaining E_1 and E_2 . This gives us four pairs of data: one containing D_1 and E_1 , one D_2 and E_1 , the next one D_1 and E_2 , and the last one D_2 and E_2 . We then do two linear interpolations on the distance for obtaining two energy deposits, maintaining the incident energy constant. Next, we do a linear interpolation over E_1 and E_2 using the two energy deposits found before, obtaining the final energy deposit. This is the energy deposit that is used in the calorimeters. We do the same procedure for obtaining the information of all secondary particles. For calculating the final quantity, as it should be an integer, we do: $Q + \sigma_Q \times RndmG$, where $RndmG$ is a random number coming from a Gauss distribution, and use the next bigger integer.

In order to generate the secondary particles, we first sort all the secondary particles by probability, from higher to lower. Then we generate a random number on a uniform distribution, if the number is bigger than the interpolated probability, we do not take into account this particle, if it is smaller, we save the particle for analyzing it in the correspondent sub detector routine. Since this has a random component, we also need to ensure energy conservation. For this, we keep a count of the energy deposited plus the energy of all particles exiting the calorimeter. If the final energy beats the incident energy, we eliminate the last secondary particles until the energy is conserved. If the final energy is not enough to cover all the incident energy, we add a particle of the type of the incident particle with the energy needed for the conservation.

As an example of the results of this simulation for energy depositions, we show in Figure 4.4 the simulation of a box of steel that would represent the ATLAS HCal barrel. On the left panel we show the normalized energy versus distance traveled by a particle of incident energy 10.5 GeV, and on the right panel the normalized energy versus incident particle energy for a particle traveling a length of 1.04 m (52.8% of the total HCal barrel width).

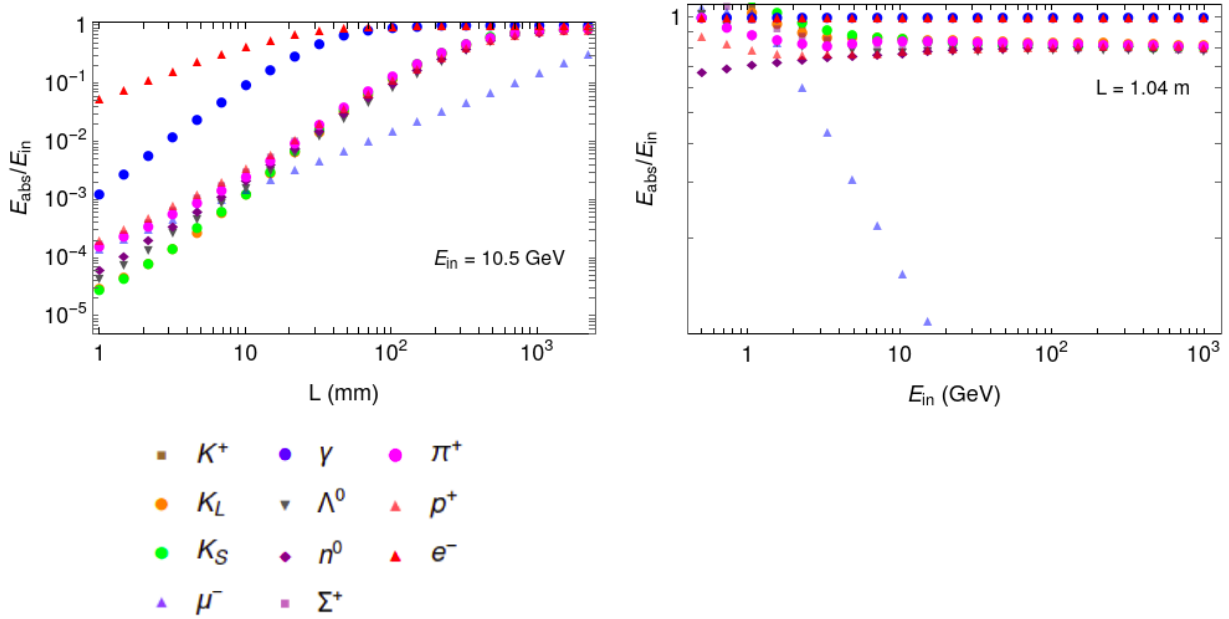


Figure 4.4: Geant4 simulation of particles through a block of steel that would represent the barrel of the ATLAS hadronic calorimeter. Left: normalized energy versus distance traveled by particle for an incident energy of 10.5 GeV. Right: normalized energy versus incident particle energy for 1.04 m length. Bottom: color code of particles included in the simulation.

With these simulations we are able to identify, with a higher precision, the deposited energy in each calorimeter and track the particles generated through all the ATLAS detector. The Toy Detector and the main program were both based in [30]. More information about it can be find in [1].

Trigger	2015	2016	2017	2018	Total
<i>High-E_T</i> CalRatio Trigger with $E_T > 60$ GeV	3	33	41	40	117
<i>High-E_T</i> CalRatio Trigger with $E_T > 100$ GeV	-	-	44	59	103
<i>Low-E_T</i> CalRatio Trigger (2016)	-	11	43	-	54
<i>Low-E_T</i> CalRatio Trigger (2018)	-	-	-	59	59

Table 4.2: CalRatio Triggers available during LHC Run 2 and the integrated luminosity (fb^{-1}) collected during each period of time (from year 2015 to 2018) and in total. Table obtained from [2].

4.3.3 Triggers and Selection

During the data collection of LHC Run 2, there were two CalRatio Triggers available: the *High- E_T* focusing on large mass particles and the *Low- E_T* focusing on small mass particles. There are two versions of each trigger, implemented in different periods of time. In our implementation we use the four triggers and adapt them to be able to simulate as best as possible the data collected by the ATLAS experiment. The triggers used by ATLAS are presented in Table 4.2 as well as the integrated luminosity collected for each in the different years and in total. We infer from the table that the *Low- E_T* 2018 trigger runs paired with the *High- E_T* 100 GeV trigger since both of them had a collected luminosity of 59 fb^{-1} the year 2018, and the *Low- E_T* 2016 trigger run paired with the *High- E_T* 60 GeV trigger in the years 2016 and 2017, since in the combination of both years, both triggers had a collected luminosity of 54 fb^{-1} . Thus, the *High- E_T* 100 GeV trigger run alone collecting 44 fb^{-1} in the year 2017 and the *High- E_T* 60 GeV trigger run alone collecting 63 fb^{-1} . In the following we will consider this assumptions for the calculations of the number of events surviving all the selection process.

4.3.3.1 Level 1 Trigger

The CalRatio triggers (*High- E_T* and *Low- E_T*) only differ from each other on the L1 trigger, the HLT is the same for both.

The High E_T L1 Trigger

Selects energy deposits (in the ECal and HCal combined) within a $\Delta\eta \times \Delta\phi$ area of 0.2×0.2 which

must be greater than 60 or 100 GeV, depending on the version.

For implementing it, we assumed the energy deposits, computationally, can be interpreted as jets, then we do a clustering of the detected particles in the ECal and HCal using FastJet with a radius (R parameter) of 0.112. We chose this parameter to generate areas similar enough to 0.2×0.2 ($\Delta\eta \times \Delta\phi$), and applied the corresponding 60 or 100 GeV cut over the total energy.

The $Low E_T$ L1 Trigger

The 2018 (2016) version of this trigger selects events where the (two) largest energy deposit(s) have a deposition on the HCal greater than 30 GeV and a deposition on the ECal smaller than 3 GeV.

For implementing the $Low E_T$ L1 triggers, we made the same assumptions as in the $High E_T$ trigger, and used FastJet to generate jets with an R parameter of 0.2, as specified in [22]. For this implementation we used the separation of energy deposited on the ECal and HCal made for each jet, and analyzed separately the depositions in each calorimeter. First we analyze the energy deposited on the HCal, if it is greater than 30 GeV, we analyze if the the energy deposited in the ECal is less than 3 GeV, if one of these requirements is not satisfied, the jet does not pass the trigger.

Since only one of these two triggers is necessary to pass to the next trigger, we implement first the $High E_T$ L1 trigger, and if passed, the event goes directly to the HLT, if it is not passed, then it goes through the $Low E_T$ L1 trigger.

4.3.3.2 High Level Trigger

If an event has already passed one of the L1 triggers, it now goes through the cuts of the HLT, presented in Table 4.3. For this trigger we will use the jets clustered inside the Toy Detector with R parameter 0.4.

All the jets of each event pass through a CalRatio jet cleaning algorithm that will eliminate signal coming form electronic or pile-up noise. We do not implement this algorithm since, as a simulation, we do not have this type of noise. Then, in each event that survives this algorithm, at least one of the jets must have: $E_T > 30$ GeV, $|\eta| < 2.5$ and $\log_{10}(E_{HCal}/E_{ECal}) > 1.2$. The last one

guarantees large depositions of energy in the HCal compared with the ECal (about 16 times) which will strongly suggest the jets coming from an LLP. We implement this by using the `eneecal` and `enehcal` variables defined in the clustering. Jets surviving these cuts are going to be the trigger jets.

Trigger jets are also required to have no tracks with $p_T > 2$ GeV in a cone of $\Delta R = 0.2$. For this requirement we designed a double loop. The first loop is over all the surviving jets. For each of these jets we do a loop over all tracks (particles detected in the ID). If the angular distance between the track and the jet being analyzed is less than 0.2, we proceed to analyze the momentum of the track, if it is greater than 2 GeV, then the jet is discarded, otherwise, it survives the cut.

For an event to pass all the pre selection process, it needs to pass the CalRatio trigger and to have at least two clean jets. The requisites for a jet to be a “clean jet” are: $p_T > 40$ GeV and $|\eta| < 2.5$. There is an additional requirement for isolation defined as $\Delta R_{min}(\text{tracks, jets})$, a variable that measures the angular distance between the jet axis and the closest track with $p_T > 2$ GeV. We require that $\Sigma \Delta R_{min}(\text{tracks, jets}) > 0.5$, where the Σ implies the summation over all clean jets with $p_T > 50$ GeV. For implementing this we designed a double loop, similar to the one used for the no tracks requirement. The first loop analyzes the surviving jets, if it has an energy greater than 50 GeV, it passes to the second loop, which analyzes all particles in the ID. Inside this loop we search for the smallest angular distance between the jet and the particle in the ID (which has to have momentum greater than 2 GeV) and save it in a variable. There is only one result per each clean jet. A summation is made over all the results, if the it is greater than 0.5, the event survives, if not it is discarded.

4.3.4 Event selection

After the pre selection, the requirements for the events to be accepted in the analysis also include: a jet-level neural network (NN) trained to distinguish signal-like jets, a per-event Boost Decision Trees (BDT) to differentiate events from background and signal, with event level variables, a trigger matching algorithm (where at least one CalRatio jet candidate must match the jet that fires the

High Level Trigger	Cuts
Jets passing the <i>CalRatio cleaning</i>	≥ 1
$(E_T)_{(j)}$	$> 30 \text{ GeV}$
$ \eta _{(j)}$	< 2.5
$\log_{10}(E_{\text{HCal}}/E_{\text{ECal}})_{(j)}$	> 1.2
Preselection	Cuts
Number of clean jets	≥ 2
$\Delta R_{\min}(\text{tracks, jets})$	> 0.5

Table 4.3: High Level Trigger cuts.

trigger) and a time window $-3 < t < 15$ ns (for avoiding background or remnants signals from another bunch crossing). We did not implement these requirements, but we simulated them by an efficiency. We obtained the average efficiency of each of the triggers for the *High- E_T* and *Low- E_T* analysis reported in the ATLAS search, and generate a random number between 0 and 1 using a uniform distribution, if the random number is greater than the efficiency obtained we discard the event, if not, the event survives and we proceed to the next requirement.

There are two algorithms for selecting the jets of this analysis: the *High- E_T* algorithm and the *Low- E_T* algorithm. We considered the *High- E_T* selection algorithm for models with $m_\phi > 200$ GeV and the *Low- E_T* algorithm for the rest. Both of them are independent of the CalRatio trigger used and use the same type of cuts but differ on the required values for each one. The NN analyzes all jets in the event and gives each of them a score reflecting the probability of them being a displaced jet coming from the an LLP decay. Then, the BDT select four jets (two for each selection algorithm), depending on the score given by the NN. There are two special requirements for these four CalRatio jet candidates: the $\log_{10}(E_{\text{HCal}}/E_{\text{ECal}})$ must be greater than -1.5, and they must not be detected on the junction between the ECal barrel and end caps ($1.45 < |\eta| < 1.55$) since the poor coverage of the ECal might produce jets with artificial low fractions of energy.

From these four jet candidates, two of them should pass the following cuts (Table 4.4). Since we cannot apply the machine learning methods, we choose the best pair of jets that correctly satisfy the requirements for reproducing the results.

Each event must contain two jets that satisfy:

<i>Low-E_T</i>	<i>High-E_T</i>
$H_T^{miss}/H_T < 0.6$ $\sum_{j_1, j_2} \log_{10}(E_{\text{HCal}}/E_{\text{ECal}}) > 2$ $p_{Tj_1} > 80 \text{ GeV}$ $p_{Tj_2} > 80 \text{ GeV}$ NN product > 0.7	$H_T^{miss}/H_T < 0.6$ $\sum_{j_1, j_2} \log_{10}(E_{\text{HCal}}/E_{\text{ECal}}) > 1$ $p_{Tj_1} > 70 \text{ GeV}$ $p_{Tj_2} > 80 \text{ GeV}$ NN product > 0.5

Table 4.4: Event selection restrictions presented for *Low- E_T* and *High- E_T* analysis.

- The ratio $H_T^{miss}/H_T < 0.6$, where H_T is defined as the scalar sum of the jets transverse momenta and H_T^{miss} as the magnitude of the vectorial sum of these jets transverse momenta (equations 4.1 and 4.2 respectively),

$$H_T = \sum_i |\bar{p}_T|_i \quad (4.1)$$

$$H_T^{miss} = |\sum_i (\bar{p}_T)_i| \quad (4.2)$$

- The sum $\sum_{j_1, j_2} \log_{10}(E_{\text{HCal}}/E_{\text{ECal}})$ must be greater than 2 for the *Low- E_T* selection and 1 for the *High- E_T* selection, j_1 and j_2 refer to the two jets selected. This ensures the fraction of energy deposition in the HCal is considerably greater than that in the ECal.
- The transverse momenta of the two jets must be greater than 80 GeV for the *Low- E_T* algorithm and for the *High- E_T* one, one greater than 80 and the other greater than 70 GeV.
- Both must satisfy a restriction on the NN product (0.7 and 0.5), but, as explained before, we will use an efficiency to cover this.

4.3.5 Background estimation

At last, for estimating the background a data-driven ABCD method is used by ATLAS. The procedure consist on creating a plane with two uncorrelated variables (one for the "x" axis and one for the "y" axis) and assuming the background can be factorized in this plane. The ΔR_{min} (tracks, jets) and the BDT score are chosen. This plane generates four regions: A, B, C and D. The events in

Scalar mass m_Φ (GeV)	LLP mass m_{τ_d} (GeV)	$c\tau$ (m)
1000	275	2.40
600	150	1.84
400	100	1.61
200	50	1.25
125	55	1.05
60	5	0.22

Table 4.5: Combination of masses of the scalar and the LLP, and $c\tau$ reported in [2], each of the six combinations are simulated and analyzed by the PUCP Toy Detector.

region A are considered to be the signal events, the ones in regions B, C and D are going to be considered background. For an event to be part of the region A in the *High- E_T* analysis is required to have a $\Delta R_{min}(\text{tracks, jets})$ greater than 1.5, and a *High- E_T* BDT score greater than 0.36. If it is part of the *Low- E_T* , the requirements are: $\Delta R_{min}(\text{tracks, jets})$ greater than 1, and a *High- E_T* BDT score greater than 0.27.

In our simulation we implemented the requirements of $\Delta R_{min}(\text{tracks, jets})$ and applied an additional efficiency due to the BDT cut. This efficiency is calculated by taking the total efficiency produce by the whole Region A cut (ΔR and BDT) given by the ATLAS experiment, and then dividing it by the efficiency generated in our simulation, containing only the implementation of the ΔR requirement. We obtained an average efficiency for the *High- E_T* selection algorithm and another for the *Low- E_T* . They are discussed in the following Section.

4.4 Results

We generated collision data for the model detailed in Section 4.2 in MadGraph5 for the six combinations of masses reported in the analyzed ATLAS search (Table 4.5) obtaining the Les Houche Event files to be processed by the PUCP Toy Detector. We applied all the triggers and cuts specified in Section 4.3.3 in the main program, as shown in the flow chart (Figure 4.2). With all this information we obtained the percentage of events surviving each cut in our detector.

As specified in Table 4.2, during different periods of time, there are different CalRatio triggers available for data collection, which collect different integrated luminosities. From this, we assume

that:

- the *High- E_T* 60 GeV trigger together with the *Low- E_T* 2016 trigger have collected a total luminosity of 54 fb^{-1} ;
- the *High- E_T* 60 GeV trigger by its own has collected an additional 63 fb^{-1} .
- Similarly, for the *High- E_T* 100 GeV trigger together with the *Low- E_T* 2018 trigger, the total luminosity collected is 59 fb^{-1} ,
- the *High- E_T* 100 GeV trigger by its own has collected an additional 44 fb^{-1} .

For this reason we run, per each combination of masses, two different sets of data of 50k events each. One is used to obtain the events surviving all the selection process applying the *High- E_T* 60 GeV or *Low- E_T* 2016, and the other applying the *High- E_T* 100 GeV or *Low- E_T* 2018.

Since we generate Φ production with and without an initial state radiation (ISR) jet, we run an algorithm for matching and merging our Pythia-generated event. This leads to having a lower total number of events to be analyzed.

Even though we have four combinations of triggers, we only used two sets of data. In each of them we analyzed one version of the *High- E_T* and one of the *Low- E_T* L1 trigger. We recognized the probability of an event passing the *High- E_T* trigger (any version) is considerably higher than that of passing the *Low- E_T* trigger (any version). This led to the conclusion that the most optimal way of running this trigger is to first run the *High- E_T* trigger; if the event survives, it proceeds to the next requirement (HLT). If it does not survive, the event passes through the *Low- E_T* trigger. If it survives, the L1 trigger is considered passed, and the event proceeds to the next requirement. If it does not survive, it is discarded.

For obtaining the total efficiency ϵ of the events surviving each of the cuts, we weighted the sum of the efficiencies of the four combinations of triggers discussed before, by using the following equation:

$$\epsilon = \frac{\sum_i \mathcal{L}_i \left(\frac{N_s}{N_g} \right)_i}{\sum_i \mathcal{L}_i}, \quad (4.3)$$

where N_s is the number of events surviving the cuts, N_g the number of generated events after matching, \mathcal{L} the collected luminosity and the sub index i represents the summation over the four combinations of CalRatio triggers.

In Tables 4.6, 4.7, 4.8, 4.9, 4.10 and 4.11 the results per cut are shown. Each table shows the results for a different combination of scalar and LLP masses. “Preselection (trigger)” refers to the percentage of events surviving the CalRatio trigger (L1 + HLT), and also the additional requirements on $\Delta R_{min}(\text{tracks, jets})$ and the presence of two clean jets. “BDT, matching, timing” refers to the events passing the restriction made by the Boost Decision Tree, in our case a unique efficiency is applied in all cases, the same as in the “NN product” entry that refers to the Neural Network product, the product of the two highest NN scores for clean jets in a given event. The “Selection” entry shows the percentage of events surviving the correspondent event selection algorithm (depending on the masses of the model being analyzed). Finally, the “Region A” entry makes reference to the percentage of events that, after all the cuts being applied, survive to the $\Delta R_{min}(\text{tracks, jets})$ and BDT requirements added by the ABCD method for background estimation. The tables show for each cut:

- Experimental results (Exp.). These are results reported on [2], given as the percentage of events surviving the respective cut. The number of total events is unspecified.
- Efficiency obtained by the PUCP Toy Detector (Eff.). It is calculated analyzing the four possible combination of CalRatio triggers by using equation 4.3. It represents the percentage of the events surviving the respective cut, given that they have survived all the requirements before.
- Number of events coming only from the *High- E_T* L1 60 GeV trigger.
- Number of events coming from the *High- E_T* L1 60 GeV and the *Low- E_T* L1 2016 triggers.
- Number of events coming only from the *High- E_T* L1 100 GeV trigger.
- Number of events coming from the *High- E_T* L1 100 GeV and the *Low- E_T* L1 2018 triggers.

It is intuitive to see that the subtraction of the quantities (L1 60 GeV + 2016) minus (L1 60 GeV) will give us the amount of additional events that are surviving to the *Low- E_T* CalRatio trigger but not the *High- E_T* trigger. The same applies for the 100 GeV and 2018 version. It might seem that there are considerably less events passing the *Low- E_T* CalRatio trigger than the ones that pass the *High- E_T* CalRatio trigger, but this is not necessarily the case. There are two principal reasons for this, we analyze the *High- E_T* trigger first, and if passed, we do not analyze the *Low- E_T* trigger, which creates the possibility of having an event that might pass the two triggers independently but will appear as passing only the *High- E_T* . The second reason is because the *Low- E_T* trigger is more restricted, the requirements for this triggers are stronger. It is also notorious that for the lowest masses, there appear to be no additional events surviving the last cut (Region A) coming from the *Low- E_T* trigger. Besides the two reasons already given, it must be noted that the statistics are really small compared to the higher masses, which might also produce these low efficiencies for the trigger.

In the tables we can also observe that the efficiency obtained by the PUCP Toy Detector in the Region A is always within the order of magnitude reported by ATLAS search. In this way we can conclude that the results are precise enough and with this the detector is validated and prepared for a future search for LLPs decaying inside the calorimeters based in any other BSM model.

	Exp.	Eff.	<i>High-E_T</i> 60 GeV	<i>High-E_T</i> 60 GeV + <i>Low-E_T</i> 2016	<i>High-E_T</i> 100 GeV	<i>High-E_T</i> 100 GeV + <i>Low-E_T</i> 2018
Preselection (trigger)	23	30,8	5968	5968	5937	5955
BDT, matching, timing	20	27	5205	5205	5245	5261
Selection	12	13,7	2630	2630	2674	2676
NN product	9,3	9,6	1868	1868	1836	1837
Region A	7,4	7,5	1484	1484	1460	1460

Table 4.6: Model with $m_\phi = 1000$ GeV and $m_{\pi_d} = 275$ GeV. Number of events run for L1 60 GeV + 2016: 19331, and number of events run for L1 100 GeV + 2018: 19345. Event selection algorithm used: *High-E_T*.

	Exp.	Eff.	<i>High-E_T</i> 60 GeV	<i>High-E_T</i> 60 GeV + <i>Low-E_T</i> 2016	<i>High-E_T</i> 100 GeV	<i>High-E_T</i> 100 GeV + <i>Low-E_T</i> 2018
Preselection (trigger)	19	24,3	5204	5204	5175	5217
BDT, matching, timing	17	21,3	4562	4562	4528	4566
Selection	9,6	10,9	2342	2342	2309	2310
NN product	6,9	7,6	1623	1623	1623	1623
Region A	4,8	5,9	1258	1258	1262	1262

Table 4.7: Model with $m_\phi = 600$ GeV and $m_{\pi_d} = 150$ GeV. Number of events run for L1 60 GeV + 2016: 21284, and number of events run for L1 100 GeV + 2018: 21453. Event selection algorithm used: *High-E_T*.

	Exp.	Eff.	<i>High-E_T</i> 60 GeV	<i>High-E_T</i> 60 GeV + <i>Low-E_T</i> 2016	<i>High-E_T</i> 100 GeV	<i>High-E_T</i> 100 GeV + <i>Low-E_T</i> 2018
Preselection (trigger)	15	19,9	4753	4753	4463	4598
BDT, matching, timing	13	17,5	4148	4148	3904	4028
Selection	6,8	7,8	1796	1796	1836	1851
NN product	4,2	5,6	1261	1261	1332	1342
Region A	2,6	4,2	963	963	998	1004

Table 4.8: Model with $m_\phi = 400$ GeV and $m_{\pi_d} = 100$ GeV. Number of events run for L1 60 GeV + 2016: 23258, and number of events run for L1 100 GeV + 2018: 23191. Event selection algorithm used: *High-E_T*.

	Exp.	Eff.	<i>High-E_T</i> 60 GeV	<i>High-E_T</i> 60 GeV + <i>Low-E_T</i> 2016	<i>High-E_T</i> 100 GeV	<i>High-E_T</i> 100 GeV + <i>Low-E_T</i> 2018
Preselection (trigger)	6,9	8	2587	2593	1785	2367
BDT, matching, timing	5,9	6,4	1926	1930	1324	1724
Selection	0,59	0,79	228	228	205	208
NN product	0,53	0,46	128	128	124	126
Region A	0,46	0,32	90	90	89	91

Table 4.9: Model with $m_\phi = 200$ GeV and $m_{\pi_d} = 50$ GeV. Number of events run for L1 60 GeV + 2016: 27501, and number of events run for L1 100 GeV + 2018: 27466. Event selection algorithm used: *Low-E_T*.

	Exp.	Eff.	<i>High-E_T</i> 60 GeV	<i>High-E_T</i> 60 GeV + <i>Low-E_T</i> 2016	<i>High-E_T</i> 100 GeV	<i>High-E_T</i> 100 GeV + <i>Low-E_T</i> 2018
Preselection (trigger)	1,1	1,5	523	525	376	475
BDT, matching, timing	0,84	1,2	385	386	278	353
Selection	0,06	0,17	61	61	43	44
NN product	0,04	0,12	42	42	33	33
Region A	0,03	0,09	31	31	22	22

Table 4.10: Model with $m_\phi = 125$ GeV and $m_{\pi_d} = 55$ GeV. Number of events run for L1 60 GeV + 2016: 30713, and number of events run for L1 100 GeV + 2018: 30936. Event selection algorithm used: *Low-E_T*.

	Exp.	Eff.	<i>High-E_T</i> 60 GeV	<i>High-E_T</i> 60 GeV + <i>Low-E_T</i> 2016	<i>High-E_T</i> 100 GeV	<i>High-E_T</i> 100 GeV + <i>Low-E_T</i> 2018
Preselection (trigger)	0,73	0,94	377	377	284	361
BDT, matching, timing	0,45	0,73	273	273	215	266
Selection	0,02	0,09	33	33	33	33
NN product	0,006	0,06	21	21	20	20
Region A	0,003	0,040	14	14	14	14

Table 4.11: Model with $m_\phi = 60$ GeV and $m_{\pi_d} = 5$ GeV. Number of events run for L1 60 GeV + 2016: 35473, and number of events run for L1 100 GeV + 2018: 35257. Event selection algorithm used: *Low-E_T*.

Chapter 5

Summary and Conclusions

In the present thesis we have used the CalRatio trigger to search for Long Lived Particles decaying into hadron jets in the calorimeters of the ATLAS detector by reproducing the results obtained by the ATLAS Collaboration [2]. We simulated the studied model in MadGraph5. It was composed by a heavy scalar field generated via gluon fusion decaying into two dark pions (the LLPs), each of them decays into a pair of fermions. We have generated two data sets of 50 000 events in MadGraph5 for each combination of masses given in Table 4.5, each of the data sets is dedicated for running one of the two different versions of the CalRatio triggers.

We have implemented all the cuts used in the search: the two CalRatio triggers, with two versions each, composed by a Level 1 trigger, a High Level Trigger and some additional cuts; and the event selection algorithms (*High- E_T* and *Low- E_T*) that will select the events that are considered candidates to signal. We also implement the cuts necessary for background estimation (which uses a data- driven ABCD method), necessary to define the region that is going to be the signal (region A). The search also applies some restrictions based on a neural network and a Boost Decision Tree. We do not apply these restrictions, but we use the results obtained by the Collaboration and use them as an efficiency.

For this implementation we have presented the construction of a simulation of the ATLAS experiment which we call the PUCP Toy Detector. It is based on all the features the ATLAS detector

has. It considers: dimensions, efficiency and resolution of each sub detector, limits on pseudorapidity and energy depositions on the calorimeters given by a Geant4 simulation. It tracks every particle in an event coming from the proton proton collision and returns the reconstructed energy, momentum, pseudorapidity and phi angle, and clusters all particles detected in the calorimeters using FastJet. The PUCP Toy Detector receives as input a Pythia8 object with the information of one the event. It is called from a main program which receives as input a Les Houche Event file. The program runs Pythia8 over the LHE and generates the hadronization. Subsequently, it calls the Toy Detector. With the information the Toy Detector returns, it analyzes the triggers and selection algorithms.

Finally, after applying all the cuts, we analyze the results obtained and we concluded that the PUCP Toy Detector reproduce, with reasonable precision, the results already obtained by the ATLAS Collaboration, so we are able to say the detector is validated and prepared to be used. This is an important achievement since we successfully accomplished to develop a tool relevant for searches of new physics, specifically of long lived particles, and is now prepared to perform a search for LLPs coming from BSM models that have not been experimentally studied before, such as an R parity violation SUSY model or one containing a Heavy Neutral Lepton (i.e. a heavy neutrino produced by the Seesaw mechanism).

Bibliography

- [1] L. X. Coll Saravia. *Desarrollo de un detector juguete basado en el experimento CMS para la búsqueda de partículas neutras con largo tiempo de vida*. 2020.
- [2] Georges Aad et al. “Search for neutral long-lived particles in pp collisions at $\sqrt{s} = 13$ TeV that decay into displaced hadronic jets in the ATLAS calorimeter”. In: *JHEP* 06 (2022), p. 005. DOI: 10.1007/JHEP06(2022)005. arXiv: 2203.01009 [hep-ex].
- [3] Scott Willenbrock. “Symmetries of the standard model”. In: *Theoretical Advanced Study Institute in Elementary Particle Physics: Physics in D 4*. Oct. 2004, pp. 3–38. arXiv: hep-ph/0410370.
- [4] Francis Halzen and Alan Martin. *Quarks & Leptons: An introductory course in modern particle physics*. New York, USA: John Wiley & Sons, 1984.
- [5] A. Caputo et al. “The seesaw portal in testable models of neutrino masses”. In: *JHEP* 06 (2017), p. 112. DOI: 10.1007/JHEP06(2017)112. arXiv: 1704.08721 [hep-ph].
- [6] A. Donini et al. “The minimal 3+2 neutrino model versus oscillation anomalies”. In: *JHEP* 07 (2012), p. 161. DOI: 10.1007/JHEP07(2012)161. arXiv: 1205.5230 [hep-ph].
- [7] Matthew D. Schwartz. “TASI Lectures on Collider Physics”. In: *Proceedings, Theoretical Advanced Study Institute in Elementary Particle Physics : Anticipating the Next Discoveries in Particle Physics (TASI 2016): Boulder, CO, USA, June 6-July 1, 2016*. Ed. by Rouven Essig and Ian Low. 2018, pp. 65–100. DOI: 10.1142/9789813233348_0002. arXiv: 1709.04533 [hep-ph].

- [8] The ATLAS Collaboration et al. “The ATLAS Experiment at the CERN Large Hadron Collider”. In: *Journal of Instrumentation* 3.08 (Aug. 2008), S08003. DOI: 10.1088/1748-0221/3/08/S08003. URL: <https://dx.doi.org/10.1088/1748-0221/3/08/S08003>.
- [9] R. L. Workman et al. “Review of Particle Physics”. In: *PTEP* 2022 (2022), p. 083C01. DOI: 10.1093/ptep/ptac097.
- [10] D. Barney. “Calorimetry in Particle Physics, and the CMS High-Granularity Calorimeter”. In: *Journal of Instrumentation* 15.07 (July 2020), p. C07018. DOI: 10.1088/1748-0221/15/07/C07018. URL: <https://dx.doi.org/10.1088/1748-0221/15/07/C07018>.
- [11] M. Livan and R. Wigmans. *Calorimetry for Collider Physics, an Introduction*. UNITEXT for physics. Springer International Publishing, 2019. ISBN: 9783030236540. URL: <https://books.google.com.pe/books?id=U3SczQEACAAJ>.
- [12] Abhigyan Dasgupta. “Search for Long-Lived Particles Decaying to Displaced Dimuons at 13 TeV and Study of Neutron-Induced Background Hits in the Muon System of the Compact Muon Solenoid”. PhD thesis. UCLA, Los Angeles (main), 2019.
- [13] Particle Data Group et al. “Review of Particle Physics”. In: *Progress of Theoretical and Experimental Physics* 2020.8 (Aug. 2020). 083C01. ISSN: 2050-3911. DOI: 10.1093/ptep/ptaa104. eprint: https://academic.oup.com/ptep/article-pdf/2020/8/083C01/34673740/rpp2020-vol2-2015-2092_18.pdf. URL: <https://doi.org/10.1093/ptep/ptaa104>.
- [14] The CMS Collaboration. “Search for long-lived particles that decay into final states containing two muons, reconstructed using only the CMS muon chambers”. In: (Apr. 2015).
- [15] Vardan Khachatryan et al. “Search for long-lived particles that decay into final states containing two electrons or two muons in proton-proton collisions at $\sqrt{s} = 8$ TeV”. In: *Phys. Rev. D* 91.5 (2015), p. 052012. DOI: 10.1103/PhysRevD.91.052012. arXiv: 1411.6977 [hep-ex].

- [16] M. Aaboud et al. “Search for long-lived particles in final states with displaced dimuon vertices in pp collisions at $\sqrt{s} = 13$ TeV with the ATLAS detector”. In: *Phys. Rev. D* 99 (1 Jan. 2019), p. 012001. DOI: 10.1103/PhysRevD.99.012001. URL: <https://link.aps.org/doi/10.1103/PhysRevD.99.012001>.
- [17] M. Aaboud et al. “Search for long-lived particles produced in pp collisions at $\sqrt{s} = 13$ TeV that decay into displaced hadronic jets in the ATLAS muon spectrometer”. In: *Phys. Rev. D* 99 (5 Mar. 2019), p. 052005. DOI: 10.1103/PhysRevD.99.052005. URL: <https://link.aps.org/doi/10.1103/PhysRevD.99.052005>.
- [18] Juliette Alimena et al. “Searching for long-lived particles beyond the Standard Model at the Large Hadron Collider”. In: *J. Phys. G* 47.9 (2020), p. 090501. DOI: 10.1088/1361-6471/ab4574. arXiv: 1903.04497 [hep-ex].
- [19] Morad Aaboud et al. “Search for long-lived, massive particles in events with displaced vertices and missing transverse momentum in $\sqrt{s} = 13$ TeV pp collisions with the ATLAS detector”. In: *Phys. Rev. D* 97.5 (2018), p. 052012. DOI: 10.1103/PhysRevD.97.052012. arXiv: 1710.04901 [hep-ex].
- [20] Albert M Sirunyan et al. “Search for long-lived particles decaying into displaced jets in proton-proton collisions at $\sqrt{s} = 13$ TeV”. In: *Phys. Rev. D* 99.3 (2019), p. 032011. DOI: 10.1103/PhysRevD.99.032011. arXiv: 1811.07991 [hep-ex].
- [21] Georges Aad et al. “Search for pair-produced long-lived neutral particles decaying in the ATLAS hadronic calorimeter in pp collisions at $\sqrt{s} = 8$ TeV”. In: *Phys. Lett. B* 743 (2015), pp. 15–34. DOI: 10.1016/j.physletb.2015.02.015. arXiv: 1501.04020 [hep-ex].
- [22] Morad Aaboud et al. “Search for long-lived neutral particles in pp collisions at $\sqrt{s} = 13$ TeV that decay into displaced hadronic jets in the ATLAS calorimeter”. In: *Eur. Phys. J. C* 79.6 (2019), p. 481. DOI: 10.1140/epjc/s10052-019-6962-6. arXiv: 1902.03094 [hep-ex].

- [23] J. Alwall et al. “The automated computation of tree-level and next-to-leading order differential cross sections, and their matching to parton shower simulations”. In: *JHEP* 07 (2014), p. 079. DOI: 10.1007/JHEP07(2014)079. arXiv: 1405.0301 [hep-ph].
- [24] Torbjörn Sjöstrand et al. “An introduction to PYTHIA 8.2”. In: *Comput. Phys. Commun.* 191 (2015), pp. 159–177. DOI: 10.1016/j.cpc.2015.01.024. arXiv: 1410.3012 [hep-ph].
- [25] Matteo Cacciari, Gavin P. Salam, and Gregory Soyez. “FastJet User Manual”. In: *Eur. Phys. J. C* 72 (2012), p. 1896. DOI: 10.1140/epjc/s10052-012-1896-2. arXiv: 1111.6097 [hep-ph].
- [26] Johan Alwall et al. “A Standard format for Les Houches event files”. In: *Comput. Phys. Commun.* 176 (2007), pp. 300–304. DOI: 10.1016/j.cpc.2006.11.010. arXiv: hep-ph/0609017.
- [27] S. Agostinelli et al. “GEANT4—a simulation toolkit”. In: *Nucl. Instrum. Meth. A* 506 (2003), pp. 250–303. DOI: 10.1016/S0168-9002(03)01368-8.
- [28] J. Allison et al. “Geant4 developments and applications”. In: *IEEE Transactions on Nuclear Science* 53.1 (2006), pp. 270–278. DOI: 10.1109/TNS.2006.869826.
- [29] J. Allison et al. “Recent developments in Geant4”. In: *Nuclear Instruments and Methods in Physics Research Section A: Accelerators, Spectrometers, Detectors and Associated Equipment* 835 (2016), pp. 186–225. ISSN: 0168-9002. DOI: <https://doi.org/10.1016/j.nima.2016.06.125>. URL: <https://www.sciencedirect.com/science/article/pii/S0168900216306957>.
- [30] G. Brooijmans et al. “Les Houches 2017: Physics at TeV Colliders New Physics Working Group Report”. In: *10th Les Houches Workshop on Physics at TeV Colliders*. Mar. 2018. arXiv: 1803.10379 [hep-ph].